

Wave-packet dynamics in pseudo-Hermitian lattices: Coexistence of Hermitian and non-Hermitian wavefronts

Alon Beck and Moshe Goldstein¹

¹Raymond and Beverly Sackler School of Physics and Astronomy, Tel Aviv University, Tel Aviv 6997801, Israel

(Dated: December 23, 2025)

This paper investigates wave-packet dynamics in non-Hermitian lattice systems and reveals a surprising phenomenon: The simultaneous propagation of two distinct wavefronts, one traveling at the non-Hermitian velocity and the other at the Hermitian velocity. We show that this dual-front behavior arises naturally in systems governed by a pseudo-Hermitian Hamiltonian. Using the paradigmatic Hatano-Nelson model as our primary example, we demonstrate that this coexistence is essential for understanding a wide array of unconventional dynamical effects, including abrupt “non-Hermitian reflections”, sudden shifts of Gaussian wave-packets, and disorder-induced emergent packets seeded by the small initial tails. We present analytic predictions that closely match numerical simulations. These results may offer new insight into the topology of non-Hermitian systems and point toward measurable experimental consequences.

I. INTRODUCTION

Non-Hermitian systems [1–5] have attracted significant interest in recent years, spanning a wide range of applications — from classical mechanical [6–8], acoustic [9–16], and photonic waves [17–22] with gain and loss to quantum atomic [23–26] and electronic systems [27–29]. They can challenge the conventional understanding of fundamental concepts. For example, the non-Hermitian skin effect [30–40], which is characterized by the exponential localization of bulk states at the system’s boundaries, disrupts the traditional bulk-edge correspondence [41–44]. In addition, the conventional Bloch-band theory must be extended with a generalized Brillouin zone to adequately represent their topological behaviors [45–47].

While most studies focus on eigenvalue properties, it has recently become clear that the dynamics of these systems can also play a significant role in understanding their properties [48–51]. Related semiclassical and quantum-geometric aspects of non-Hermitian wave-packet dynamics have also been explored in Refs. [52–55]. Given the complexity of the spectrum, the system’s time evolution can exhibit non-trivial behaviors, such as the dominance of specific eigenstates due to non-Hermitian skin effect [56], and peculiar wave-packet behavior near the boundaries [48].

In this paper, we will investigate in particular the dynamics of systems described by a pseudo-Hermitian Hamiltonian [57, 58]. Such Hamiltonians have the property $H^\dagger = \eta^{-1} H \eta$, where η is a positive-definite operator. This class includes, in particular, all diagonalizable Hamiltonians with parity-time (PT) symmetry [59–62]. We will show that such systems presents not only the typical exponentially increasing wave-packet dynamics [56], but also a *Hermitian* wave-packet, co-existing with the former. This coexistence arises naturally from the pseudo-Hermiticity of the Hamiltonian and leads to Hermitian wave-packets that reflect from the boundaries behavior that, in turn,

governs the boundary dynamics of the non-Hermitian wave-packet. To demonstrate the properties discussed above, we will focus primarily on the simple Hatano-Nelson model, analyzing it both numerically and analytically. However, these results can also be generalized to other pseudo-Hermitian systems.

The rest of the paper is organized as follows: In Section II, we begin by demonstrating how the existence of a transformation that makes the Hamiltonian Hermitian (a condition equivalent to pseudo-Hermiticity [63]) implies the coexistence of two types of dynamics: Hermitian and non-Hermitian. We show how this transformation is derived within the Hatano-Nelson model.

In Section III, we investigate the non-Hermitian dynamics of Gaussian wave-packets, focusing on cases with small ($\sigma \ll a$) and moderate ($a < \sigma \ll L$) wave-packet width σ (a and L being the lattice spacing and system size), as detailed in Sections IIIA and IIIB, respectively. While the coexistence of the two wave-packets is observed in both scenarios, the case of $a < \sigma \ll L$ can exhibit additional, unexpected behavior, such as: (a) an abrupt change in velocity resulting from the reflection of the Hermitian wave-packet at the wall; and (b) a sudden spatial “jump” of the wave-packet, caused jointly by this reflection and by the finite maximal velocity on the lattice. The latter effect produces two wavefronts that propagate side by side — at a certain point, the reflected front can overtake the original one, giving rise to the striking apparent “jump” in the wave-packet’s position.

In Sec. IIIC, we examine the effect of weak disorder, showing that it can likewise induce a transition — an abrupt change in the wave-packet’s position — but now instead of arising from reflection, it originates from the small initial tails generated by the disorder.

Finally, in Sec. IV, we discuss how our results can be applied to the non-Hermitian SSH model [41, 64, 65], demonstrating that our findings extend to other pseudo-Hermitian Hamiltonians. We conclude by examining the implications of our results and outlining directions for

future research. Some technical details are relegated to the Appendixes.

II. DERIVING DYNAMICS VIA LOCAL TRANSFORMATION

A. Dynamics via transformation

Consider a pseudo-Hermitian Hamiltonian H , where $H^\dagger = \eta^{-1}H\eta$ for some positive-definite η . By choosing $S = \sqrt{\eta}$, we can transform the Hamiltonian to its Hermitian counterpart

$$H' = S^{-1}HS, \quad (1)$$

where $H' = H^\dagger$. We can notice now that the time-development of any wavefunction ψ can be written as [48]

$$\langle m | e^{-iHt} | \psi(0) \rangle = \langle S^\dagger m | e^{-iH't} | S^{-1}\psi(0) \rangle, \quad (2)$$

where $H' = S^{-1}HS$. This result allows us to obtain the dynamics by simply calculating the time-development of $S^{-1}\psi(0)$ in respect to the *Hermitian* Hamiltonian H' , and using S^\dagger again at the end. Since it is easier to calculate the propagator of a Hermitian system, Eq. (2) offers a valuable method to calculate the dynamics of the non-Hermitian system. However, our main observation is more subtle: Eq. (2) actually reveals the *coexistence* of two distinct types of dynamics — Hermitian and non-Hermitian. We will now investigate this coexistence in details within the Hatano-Nelson model.

B. The model

The paradigmatic Hatano-Nelson Hamiltonian [66] is the simplest model which displays most of the peculiarities of the non-Hermitian dynamics studied here. It is a 1D tight binding model with non-reciprocal hopping, given by

$$H = \sum_n t_l |n\rangle \langle n+1| + t_r |n+1\rangle \langle n|, \quad (3)$$

where $n = 1, \dots, N$. We assume that t_l and t_r are real and share the same sign, so that the Hamiltonian is pseudo-Hermitian [67]. For periodic boundary conditions (PBC), the wavefunctions are the well known Bloch waves $\langle n | k_m \rangle = \frac{1}{\sqrt{N}} e^{ik_m n}$, where a is the lattice constant and $k_m = \frac{2\pi}{a} \frac{m}{N}$, $m = 0, 1, \dots, N-1$. The energies are given by

$$E(k) = (t_l + t_r) \cos(ka) + i(t_l - t_r) \sin(ka). \quad (4)$$

For open boundary conditions (OBC), the eigenstates and spectrum are given by

$$\langle n | \psi^{(m)} \rangle = r^n (e^{i\theta_m n} - e^{-i\theta_m n}), \quad E_m = 2\sqrt{t_r t_l} \cos(\theta_m), \quad (5)$$

where $r = \sqrt{\frac{t_r}{t_l}}$, $\theta_m = \pi \frac{m}{N+1}$ [46] (where we assumed $t_l > t_r > 0$). We note that for OBC all of the eigenstates are localized on one the left edge of the system. This feature is the well-known non-Hermitian skin effect [30–40], arising due to asymmetric couplings.

As was shown above, the spectrum and the eigenstates in the cases of PBC and OBC are very different. However, it should be noted that if the system is large enough, the locality of the Hamiltonian implies that the dynamics of the bulk of the system is independent of the boundary conditions, which affect only wave-packets approaching the boundaries. We will focus on the case of OBC, which we show below to be pseudo-Hermitian, and whose boundary structure gives rise to intriguing phenomena in the dynamics in their vicinity, as discussed later. In this case, the localization of the wavefunction in Eq. (5) can be “undone” using a diagonal non-unitary similarity transformation [45]

$$\langle n | S | m \rangle = \delta_{n,m} r^n, \quad (6)$$

where $\delta_{n,m}$ is the Kronecker delta and $r = \sqrt{\frac{t_r}{t_l}}$ as before. After the transformation (1), the Hamiltonian becomes

$$H' = \sqrt{t_l t_r} \sum_n |n\rangle \langle n+1| + |n+1\rangle \langle n|, \quad (7)$$

that is, we get a simple tight-binding Hermitian Hamiltonian with a hopping amplitude $\sqrt{t_l t_r}$. We note that this also implies that the Hamiltonian is pseudo-Hermitian by choosing $\eta = SS^\dagger$.

Using a transformation S of the type of Eq. (6), and using the observation from Eq. (2), the time-development can be written as

$$\langle m | e^{-iHt} | \psi(0) \rangle = r^m \langle m | e^{-iH't} | S^{-1}\psi(0) \rangle \quad (8)$$

That is, the non-Hermitian wave-packet can be obtained by calculating first the Hermitian dynamics of $S^{-1}\psi(0)$ and multiplying by the exponential factor r^m in the end. Therefore, the the non-Hermitian wave-packet is a manifestation of the *tail* of the Hermitian wave-packet. As we will see, the velocity and exponential growth of the non-Hermitian wave-packet peak make it more prominent than its Hermitian counterpart. However, if we look at some fixed point at space, the behavior in late times would usually be governed by the Hermitian wave-packet dynamics. In addition, only the Hermitian wave-packet is capable of reflecting from the edges of the system (or potential barriers); this fact would prove to be crucial for the analysis of wave-packet dynamics near the edges.

III. NON-HERMITIAN WAVE-PACKET DYNAMICS

We will now examine and demonstrate the differences between the two coexisting dynamics in the Hatano-Nelson model with OBC. The initial conditions of the

wave-packet will be taken as a Gaussian with width σ and average quasi-momentum k_0 , focusing on two cases: $\sigma \ll a$ (equivalent to a delta-function $\langle n | \psi(t=0) \rangle = \delta_{n,x_0}$) and $a < \sigma \ll L$, where $L = Na$. We will demonstrate the presence of coexisting dynamics in both cases and show that certain intriguing phenomena (such as emerging wave-packets) are observed only in the second case, when the width exceeds a critical threshold $\sigma > \sigma_c$. Finally, we will show that these results extend beyond the HN model, provided the Hamiltonian is pseudo-Hermitian.

A. Single-site initial condition ($\sigma \ll a$)

Here we will focus on the case where the initial condition is $|\psi(t=0)\rangle = |n\rangle$, with n representing a lattice site. We will demonstrate the coexistence of two wave-packets, showing that only the Hermitian one is responsible for the oscillations that are being observed in the system. We begin with an analytical investigation of the dynamics. Using Eq. (2), we can write

$$\langle m | \psi(t) \rangle = r^{m-n} \langle m | e^{-iH't} | n \rangle, \quad (9)$$

where the Hermitian Hamiltonian H' is given by Eq. (7). The propagator of the Hermitian Hamiltonian is given by

$$\langle m | e^{-iH't} | n \rangle = \frac{1}{N} \sum_k e^{ika(m-n)} e^{-2it_0 \cos(ka)t}, \quad (10)$$

where $t_0 = \sqrt{t_r t_l}$ is the hopping amplitude of H' . If N is large, we can replace the sum by an integral and get

$$\langle m | \psi(t) \rangle = \frac{1}{2\pi} r^{m-n} (-i)^{m-n} J_{m-n}(2t_0 t), \quad (11)$$

where $J_n(x) = \frac{1}{2\pi} \int_{-\pi}^{\pi} e^{i(ny - x \sin y)} dy$ is the Bessel function of the first kind. We can now calculate the velocities of the Hermitian and non-Hermitian wave-packets: In the case of the Hermitian Hamiltonian H' , the maximal velocity v_h is given as usual by $\max(\frac{\partial E}{\partial k})$, which is obtained for $k_m = \pm \frac{\pi}{2a}$. Therefore,

$$v_h = \pm 2a\sqrt{t_r t_l}. \quad (12)$$

However, since the non-Hermitian spectrum (given by Eq. 4) is complex, the amplitude of each eigenstate obtains a factor of $e^{\text{Im}(E)t}$, making only $\max(\text{Im}E)$ significant at long times. Therefore, the non-Hermitian velocity is given by $v_{nh} = \text{Re} \frac{\partial E}{\partial k} \Big|_{k=k_m}$, for k_m that maximize $\text{Im}E(k)$ [56]. We can see that in this case $k_m = -\pi/2$ also, and therefore

$$v_{nh} = -a(t_r + t_l). \quad (13)$$

We note that for any values of t_r, t_l , the non-Hermitian velocity will be larger than the Hermitian one.

We now proceed to numerical simulations, obtained by computation of the propagator e^{-iHt} . We note

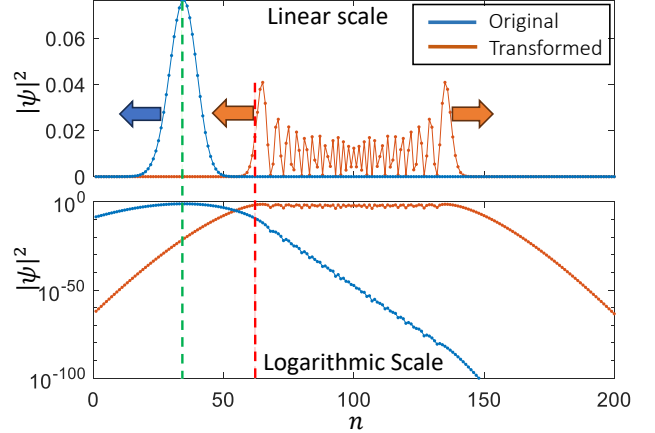


FIG. 1. Snapshot of the non-Hermitian dynamics with and without the transformation (the arrows indicate the direction of propagation of the wave-packets). See Video_1 in the Supplementary Material for an animation of the dynamics. Blue dataset: A wave-packet with initial conditions $\langle n | \psi(t=0) \rangle = \delta_{n,x_0}$, where $x_0 = N/2$, evolved numerically to time $t = 60$ with the non-Hermitian Hamiltonian, with $t_l = 2, t_r = 0.2$ (OBC). For convenience, the wave-packet is normalized to 1 (otherwise, it would present an exponential growth). Orange dataset: the same data after the transformation $y_n \rightarrow y_n r^{-n}$ (and normalization). The green/red dotted lines are the predicted positions of the fronts of the Hermitian and non-Hermitian wave-packets: $x_0 - v_{nh} t$ (green) and $x_0 - v_h t$ (red). The number of sites is $N = 200$, and the lattice spacing is $a = 1$.

that the computer precision may introduce an effective disorder term. Due to the non-Hermitian nature of the system, even weak disorder can influence the dynamics at late times (for more details see Sec. III C). To avoid such terms, one needs to increase the precision — in Matlab, for example, this can be achieved using the arbitrary precision library Advanpix [68]. Fig. 1 presents an example of a wave-packet with the initial condition $\langle n | \psi(t=0) \rangle = \delta_{n,x_0}$, where $x_0 = N/2 = 100$, propagated numerically (up to the time given in the caption), with and without the transformation, Eq. (6). We can see that without the transformation (blue data), the non-Hermitian system exhibits a wave-packet moving to the left (with exponentially-increasing amplitude, which is not apparent here only since the wave-packet is normalized). With the transformation (orange data), it is clear that the dynamics becomes Hermitian, displaying a symmetrical behavior of two wave-packets moving in opposite directions (the oscillations in between are the typical behavior we get from the Bessel-function propagator [69]). The green/red dotted lines represent the predicted position of the wave-packets due to non-Hermitian/Hermitian velocities, given by Eq. (13), (12), respectively. We can gain more insights by looking at the same picture in log-scale (bottom panel); we see that the Hermitian wave-packet does not disappear after the

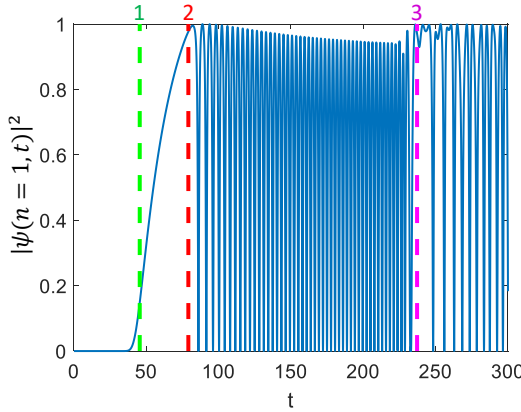


FIG. 2. Numerical results of the amplitude at the leftmost site as a function of time in the same setup as Fig. 1. Recalling that $x_0 = N/2$, three timestamps are marked by $t_1 = \frac{x_0}{v_{nh}} \approx 45$ (green), indicating the time when the non-Hermitian wave-packet hits the edge, $t_2 = \frac{x_0}{v_h} \approx 79$ (red), when the Hermitian wave-packet hits the edge, and $t_3 = \frac{2N-x_0}{v_{nh}} \approx 237$ (purple), when the Hermitian wave-packet (that went to the other side) hits the edge after being reflected from the other end.

transformation, but can be still found in the tail of the non-Hermitian wave-packet.

In Fig. 2 we provide another evidence for the significance of the Hermitian wave-packet in the non-Hermitian dynamics, by tracking the amplitude of the wave-packet at the left edge. At time t_1 , the non-Hermitian wave-packet reaches the edge at first and sticks to it. Later, at time t_2 , the front of the Hermitian wave-packet also arrives and becomes more dominant. Finally, at time t_3 , we can also see the front of the Hermitian wave-packet that went to the other side and was reflected from the opposite edge. Using the non-Hermitian and Hermitian velocities given by Eq. (13), (12), and recalling that the initial position is the center ($N/2$), we can predict that $t_1 = \frac{N/2}{v_{nh}}$, $t_2 = \frac{N/2}{v_h}$, and $t_3 = \frac{3N/2}{v_{nh}}$, which fit well to the numerical results as shown in the figure. For demonstration, see also the animation of Fig. 1.

To sum up, in the above analysis we have shown that a simple initial condition of a delta-function creates a non-Hermitian wave-packet moving to the left (since $t_l > t_r$) with velocity v_{nh} , and a Hermitian wave-packet with lower velocity v_h living alongside it. At early times, the non-Hermitian wave-packet is larger by several orders of magnitude than the Hermitian wave-packet (making the latter visible only in log-scale). However, if we probe the edge at later times, the Hermitian wave-packet will eventually arrive and govern the behavior at the boundary. Moreover, in contrast to the non-Hermitian wave-packet that propagates only in a single direction, the Hermitian wave-packets are capable of reflecting from the edges. We can understand this by recalling that the propagator is obtained from Hermitian dynamics

multiply by an exponential factor, as shown by Eq. (9). It is worth noting that even though any dynamics on the right edge is suppressed by the exponential factor, it remains relevant since the Hermitian wave-packets can probe it: While the wave-packet moving to the right is indeed exponentially suppressed, when it reaches the right boundary, it will switch direction and start being amplified back as it moves to the left (until it reaches its maximum value on the left boundary, see timestamp t_3 in Fig. 2 for example).

B. Gaussian wave-packets ($a < \sigma \ll L$)

We will now investigate the second case, where the initial conditions are Gaussian. First, we will derive a general expression for the position of the wave-packet in the bulk of the lattice and compare it to the result in the continuum. Next, we will demonstrate that an “emergent wave-packet” can be observed due to reflection from the wall, and show that the *Hermitian* wave-packet is the one that determines the time it occurs. Finally, we will discuss the critical threshold $\sigma_{c,\text{ref}}$, above which such phenomena can be observed.

1. Dynamics in the bulk

We consider a Gaussian wave-packet initial condition:

$$|\psi(t=0)\rangle = \sum_n \frac{1}{\sqrt{4\pi\sigma^2}} e^{-\frac{a^2(n-n_0)^2}{4\sigma^2} + i k_0 a n} |n\rangle. \quad (14)$$

First, we will use Eq. (2) to obtain an analytical expression for the dynamics. By completing the square we get that

$$|S^{-1}\psi(0)\rangle = C \sum_n \frac{1}{\sqrt{4\pi\sigma^2}} e^{-\frac{a^2(n-\tilde{n}_0)^2}{4\sigma^2} + i k_0 a n} |n\rangle, \quad (15)$$

where

$$C = \exp\left(\frac{\sigma^2}{a^2} \ln^2 r - n_0 \ln(r)\right), \quad \tilde{n}_0 = n_0 - \frac{2\sigma^2}{a^2} \ln r. \quad (16)$$

That is, after the transformation we obtain (up to some prefactor) a Gaussian with the same width but a shifted expectation value \tilde{n}_0 . Therefore, to proceed we need to compute the Hermitian dynamics of the Gaussian $|S^{-1}\psi(0)\rangle$ in respect to the Hamiltonian H' in Eq. (7) and then use the inverse transformation. In Appendix A we use the saddle point approximation (for large times, $t \gtrsim 1/\sqrt{t_r t_l}$) to derive an expression for the Hermitian dynamics of a Gaussian on a lattice. Using Eq. (A20), we find that

$$e^{-iH't} |S^{-1}\psi(0)\rangle \approx \tilde{C} \sum_m e^{-\frac{\sigma^2}{a^2} \left(\arcsin\left(\frac{a(m-\tilde{n}_0)}{t v_h}\right) - a k_0 \right)^2} |m\rangle, \quad (17)$$

where \tilde{C} is some constant and $v_h = 2a\sqrt{t_r t_l}$ is the maximum Hermitian velocity as defined before. Finally, we get

$$\langle m | e^{-iHt} | \psi(0) \rangle \approx \tilde{C} r^m e^{-\frac{\sigma^2}{a^2} \left(\arcsin\left(\frac{a(m-\tilde{n}_0)}{t_r v_h}\right) - a k_0 \right)^2}. \quad (18)$$

To analyze the approximation, we can expand it in powers of $t \frac{v_h}{a}$. In Appendix B we find that

$$m_{\max} \approx \tilde{n}_0 + 2\sqrt{t_r t_l} \sin(ak_0)t + \frac{2t_r t_l}{(\sigma/a)^2} \cos^2(ak_0) \ln(r)t^2, \quad (19)$$

where m_{\max} is the position of the maximum of the non-Hermitian wave-packet. That is, to second order the wave-packet is just moving with the initial k_0 -dependent velocity $2\sqrt{t_r t_l} \sin(ak_0)$, while exhibiting an acceleration of $\frac{4t_r t_l}{(\sigma/a)^2} \cos^2(ak_0) \ln(r)$.

An analysis of the continuum limit ($a \rightarrow 0$) is presented in Appendix C; we show that the non-Hermitian Hamiltonian reads

$$H = E_0 - \frac{1}{2m} \partial_x^2 + b \partial_x, \quad (20)$$

where

$$m = \frac{1}{2a^2 \sqrt{t_l t_r}}, \quad b = a \ln\left(\frac{t_r}{t_l}\right) \sqrt{t_l t_r}, \quad (21)$$

In addition, terms beyond $(t \frac{v_h}{a})^2$ in the expansion of Eq. (18) vanish, and Eq. (19) becomes

$$x_{\max}(t) = x_0 + \frac{k_0}{m}t + \frac{b}{m\sigma^2} \frac{t^2}{2}, \quad (22)$$

in agreement with the result of Li and Wan [48].

In Fig. 3 we present numerical results of the dynamics of a Gaussian wave-packet on the lattice and compare the results to the approximation in Eq. (18), and the continuum limit solution in Eq. (22). Initially, we can see that the lattice wave-packet has a similar acceleration to that of the continuum. However, for large times, only the velocity of the lattice wave-packet's peak saturates to a limiting velocity v_{nh} (as we expect for any initial condition, since there is an upper bound on the lattice velocity). We note that the approximation, Eq. (18), agrees with the numerical results, although it shows a slight deviation in the long-time limit. The reason for this is that our saddle-point approximation was constructed only in the regime $|v| < v_h$, so it enforces v_h as the maximal velocity and cannot capture the true non-Hermitian front velocity v_{nh} ; see Appendix A for more details.

2. Non-Hermitian Reflection

In the previous section we analyzed the dynamics of a Gaussian wave-packet on the lattice, and saw that

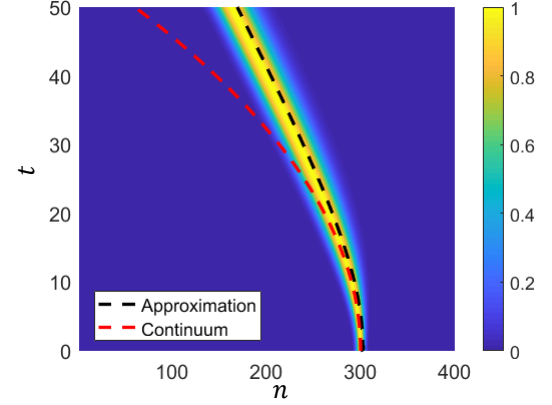


FIG. 3. Numerical results comparing the non-Hermitian dynamics of a Gaussian wave-packet on the lattice versus the continuum limit. While the initial acceleration is similar in both cases, only the lattice dynamics eventually saturates to a maximum velocity. See Video 2 in the Supplementary Material for an animation of the dynamics. The initial conditions are $n_0 = 300$, $k_0 = 0$, $\sigma = 3$, the lattice spacing is $a = 1$, and the parameter of the Hamiltonian are $t_l = 2$, $t_r = 1.5$. For the ease of presentation, the wave-function is normalized such that $\max(|\psi_n|^2) = 1$ for any t . The black and red dotted-lines represent the approximation and the continuum limit given by Eq. (18), (22) respectively.

its velocity is bounded, unlike the continuum case. We will now show that reflections from the edge can lead to even more striking differences between the lattice and the continuum. In Fig. 4 we can see a scenario similar to that of Fig. 3, with the only difference being that $k_0 = \pi/4$ instead of 0, that is, the initial velocity is to the right. We observe that the presence of the wall causes a sudden change in the behavior of the wave-packet. In the continuum, there is only a sharp change in the velocity. However, on the lattice, the jump is in the *position* of the wave-packet.

We will begin by analyzing the behavior in the continuum: At first, we can see that the non-Hermitian wave-packet accelerates to the left. It is already moving away from the wall, but then exhibits a sudden change in behavior at $t_{\text{hit}} = \frac{100}{v_0} \approx 37$, where $v_0 = 2\sqrt{t_r t_l} k_0$, which is precisely when the Hermitian wave-packet hits the wall (see Appendix C). The reason for this is that at this point the Hermitian wave-packet changes its momentum from k_0 to $-k_0$, leading to an abrupt change of $2k_0/m$ in the velocity of the *non-Hermitian* wave-packet (marked in red), since it is derived from the Hermitian wave-packet [48] — see Eq. (19). However, it is worth emphasizing that this is not the result of scattering from the wall of the non-Hermitian wave-packet itself (as it never even reached the wall), but rather its Hermitian component: In fact, such scattering can occur regardless of how far the non-Hermitian wave-packet is from the edge (as long as the Hermitian counterpart hits the wall) [70].

We now turn to discuss the case of the lattice, where

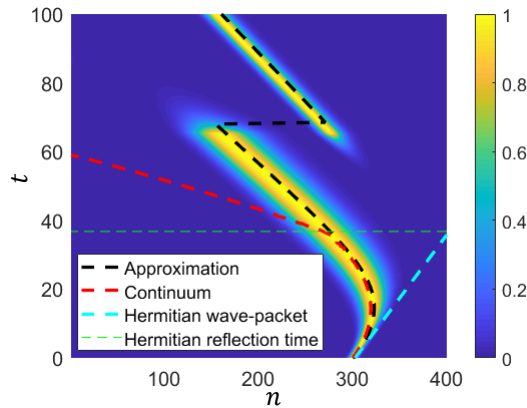


FIG. 4. Numerical results of a Gaussian wave-packet, with initial parameters identical to those of Fig. 3, except for k_0 which is now $\pi/4$ instead of 0. of propagation of the wave-packets). See Video_3 in the Supplementary Material for an animation of the dynamics. The behavior of the wave-packets in the continuum and on the lattice is similar until the time when the Hermitian wavepacket (marked in cyan) hits the wall: $t_{\text{hit}} = \frac{100}{v_0} \approx 37$ (marked in green), where $v_0 = 2\sqrt{t_r t_l} k_0$. The approximation (marked in black) was calculated using the image method, and is in agreement with the numerical results.

the reflection process is somewhat more complex. Up to the time $t_{\text{hit}} \approx 37$, the lattice and continuum systems exhibit similar behaviors. However, while at t_{hit} the continuum system changes its velocity abruptly, on the lattice it remains the same until a peculiar event happens at much larger time, around $t \approx 70$. One may suspect that this is related to the fact that the time when the Hermitian wave-packet hits the wall is different on the lattice. But this is certainly not the case, as this time is given by $t_{\text{hit}}^{\text{lattice}} = \frac{100}{2\sqrt{t_r t_l} \sin(k_0)} \approx 41$. We also emphasize that this is not a numerical artifact of some sort, as this result is supported by our approximate analytical solution (see black dotted line). The actual explanation is tied to the asymmetry of the wave-packet, arising from the velocity limit on the lattice.

Since there is an upper velocity bound on the lattice, any Gaussian with a non-zero value for k_0 will not remain symmetric as it evolves over time [69]. Intuitively, this is because the velocity range to the right of the wave-packet's peak $[v_0, v_{\text{max}}]$, differs from the range $[-v_{\text{max}}, v_0]$ to the left. This contrasts with the continuum case, where the Gaussian remains symmetric for any t . This is demonstrated in Fig. 5, where we plot a wave-packet moving toward the wall (in blue), on the lattice and in the continuum. To understand the mechanism of the reflection, it is useful to consider also the image wave-packet (with respect to the wall at $n = 400$) which is presented in red (note that the actual wave-packet hitting the wall, which is the sum of the incident and the image wave-packets, is not depicted). The key point is that until the wave-packet hits the wall ($t < t_{\text{hit}}$) there

is no significant difference between the lattice and the continuum cases. However, at the time of impact ($t = t_{\text{hit}}$), in the continuum the incident and the image wave-packets align precisely (being completely symmetric with respect to their center), unlike the behavior on the lattice. A direct consequence of this simple observation is that the non-Hermitian counterparts (presented in dashed line in the figure) of the incident and image wave-packets also align exactly at $t = t_{\text{hit}}$ in the continuum case (since they are obtained using a local transformation, the non-Hermitian wave-packets will align if and only if the Hermitian wave-packets align). Indeed, this explains the fact that $t = t_{\text{hit}}$ is the exact moment when the non-Hermitian wave-packet changes its velocity, as seen in Fig. 5.

However, on the lattice, a more subtle behavior occurs for $t > t_{\text{hit}}$: The asymmetry of the wave-packet leads to the formation of two distinct regions. In one region (represented as the blurred area in the lower-left panel of Fig. 5), we continue to observe only the tail of the incident wave-packet that has already struck the wall. In contrast, in the other region (represented by the rest of the area up to the wall which is not blurred), we already see the front of the image wave-packet which is actually the wave-packet that was reflected from the wall. An alternative perspective is that, due to the velocity limit on the lattice, the event of a “wave-packet hitting the wall” does not propagate instantaneously to all of space, in contrast with the continuum. Either way, the two regions in the Hermitian wave-packet also correspond to two regions in the non-Hermitian dynamics. In fact, as can be seen in the bottom-left panel of the figure, in each region a different non-Hermitian wave-packet is dominant. Therefore, we see now that the behavior that was observed earlier in Fig. 4, where the wave-packet “vanished” at a certain point and reappeared somewhere else, is actually just the right non-Hermitian wave-packet becoming more dominant than the left one (and since the wave-function is normalized, this means that the left wave-packet will be suppressed at this point and become invisible). Actually, looking at this in log-scale we will be able to see both of the wave-packets even for $t > 80$; see the accompanying animation for Fig. 4 for more details.

We note that as the lattice spacing decreases, the “transition time” (that is, the time where the image wave-packet becomes more dominant) approaches t_{hit} , the time in continuum limit. In Appendix D we use our approximation of Eq. (18) to show in general that for small a , this time is given by

$$t = t_{\text{hit}} + t_{\delta}, \quad (23)$$

where

$$t_{\text{hit}} = \frac{d}{\frac{\sin(ak_0)}{a} a_0^2 \sqrt{t_{l,0} t_{r,0}}}, \quad (24)$$

is the Hermitian transition time, and the leading

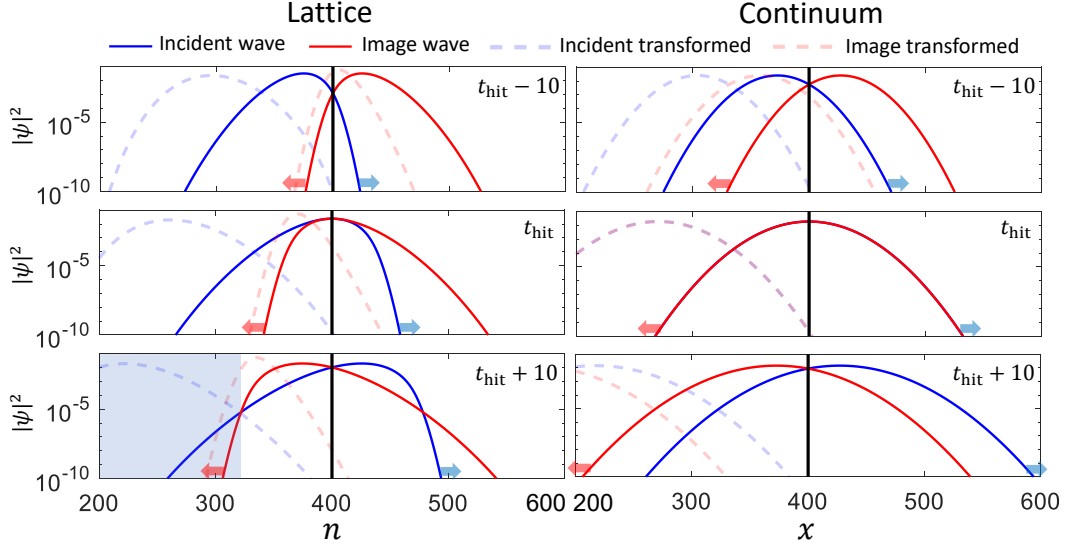


FIG. 5. A Hermitian Gaussian wave-packet (in blue) and its image (in red) moving towards a wall at $n = 400$, on the lattice (left column) and in the continuum (right column). The rows represent the timestamps: $t_{\text{hit}} - 10$, t_{hit} , $t_{\text{hit}} + 10$ (top, middle, bottom, respectively), where t_{hit} is the time where the packet hits the wall ($t_{\text{hit}} = \frac{d}{2\sqrt{t_r t_l} \sin(k_0)}$ on the lattice and $t_{\text{hit}} = \frac{d}{2\sqrt{t_r t_l} k_0}$ in continuum, where $d = 100$). The dashed lines present the results of the transformation (6), normalized to 1, which gives the non-Hermitian wave-packets that is derived from the incident and image Hermitian counterpart, respectively. See Video 4 in the Supplementary Material for an animation in the case of the lattice. The setup is the same as in Fig. 5 (note that $a = 1$ is used, so that n on the lattice is equivalent to x in continuum).

correction in terms of a is

$$t_\delta \approx \frac{3}{64} \frac{\ln^2\left(\frac{t_{r,0}}{t_{l,0}}\right)}{\sqrt{t_{l,0} t_{r,0}}} \frac{\cos^2(ak_0)}{(\sin(ak_0)/a)^3} \frac{d^3}{a_0^4 \sigma^4} a^2, \quad (25)$$

where d is the initial distance from the wall, a_0 is a fixed reference lattice spacing used to define the continuum limit (we keep $a_0^2 \sqrt{t_{l,0} t_{r,0}} = a^2 \sqrt{t_l t_r}$ constant as $a \rightarrow 0$), and $t_{r,0}, t_{l,0}$ are the right and left hopping parameters corresponding to a_0 — see Appendix C for more details.

3. Critical threshold $\sigma_{c,\text{ref}}$

It turns out that such an abrupt change in the wave-packet position can only be observed if its initial width σ exceeds a certain threshold. We will outline the main idea here, with further details presented in Appendix D 1. To understand why this occurs, we can use reasoning similar to that used for calculating the transition time in Eq. (25). In the presence of a wall, there are two wave-packets: the original and its image, induced by the wall. As discussed earlier, both wave-packets initially accelerate to the left but with opposite quasi-momentum k_0 . The image wave-packet starts with an initial amplitude that is lower by a factor of r^{2d} . As discussed above, the wave-packets on the lattice do not accelerate indefinitely, but eventually reach a finite velocity. When both wave-packets achieve this limiting velocity, their amplitudes will continue to grow at the

same rate, and their ratio will remain constant from that point onward. Therefore, for the image wave-packet to become more dominant than the real wave-packet, it must outpace it early on. Whether this occurs is highly sensitive to the initial conditions of σ and the initial distance from the wall d due to the following reason: the smaller σ is in real space, the larger the non-Hermitian acceleration becomes (see Eq. (22)), causing the wave-packet to quickly saturate at the limiting value. Another way to understand this is that the smaller σ is, the larger the initial condition for the most significant momentum component ($-\pi/2$ in our case), reducing the time it takes to reach the limiting velocity. For instance, if $\sigma = 0$ (a single-site starting condition), the wave-packet begins with the final non-Hermitian velocity, and since the image wave-packet also starts at this limiting velocity, it will never overtake the original. Therefore σ must exceed a certain value to allow the image wave-packet enough time to catch up with the original. We also note that a larger d increases their initial difference (by r^{2d}), requiring σ to be even larger. This behavior is also illustrated in Fig. 10 in Appendix D 1.

C. Effects of weak disorder

In this section, we investigate the effect of weak disorder, which does not localize the wave-packet on the scale of the system size. Related work on “non-Hermitian jumps” considers strong disorder which leads to Anderson

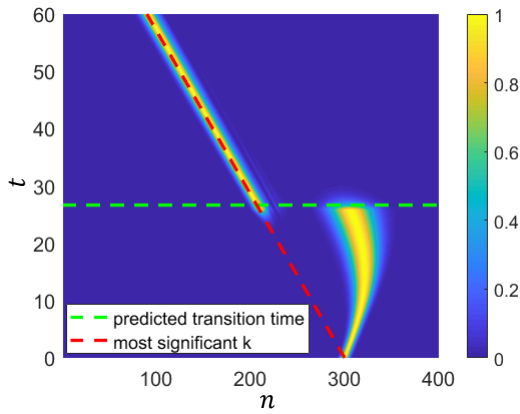


FIG. 6. Numerical results of a Gaussian wave-packet, with initial parameters identical to those of Fig. 4, except that the Hamiltonian also contain an onsite disorder realization taken from a distribution with $w = 10^{-7}$. Unlike Fig. 4, where the transition was due to the existence of the wall, here it is the result of the disorder. See Video_5 in the Supplementary Material for an animation of the dynamics. The dashed green line represents the predicted transition time $t \approx 27$, calculated as described in the main text. The dashed red line indicates the most significant k wave-packet, which becomes more prominent at the transition time.

localization, and thus addresses a different parameter regime [71–78]. While weak disorder barely alters the dynamics in Hermitian systems, we will show that in non-Hermitian systems, it can lead to the emergence of a wave-packet, similar to the effect seen earlier (caused by the reflection of the Hermitian wave-packet from the wall). However, in this case, the cause is the disorder. As we will discuss in detail below, the main reason for this behavior is that in non-Hermitian systems, the tail of the wave-packet in position space (typically insignificant in Hermitian systems) dominates the long-time dynamics due to the transformation in Eq. (6). From another perspective, weak disorder causes weak scattering to all k -states, but even small occupations of certain k -states will grow exponentially in non-Hermitian systems. This phenomenon occurs only when the initial width of the wave-packet exceeds a certain threshold, denoted as $\sigma_{c,\text{dis}}$, which depends on the disorder strength and differs from the previously discussed critical value $\sigma_{c,\text{ref}}$.

A typical way of introducing disorder is to consider an additional on-site term to the Hamiltonian: $H' = \sum_n w_n |n\rangle \langle n|$, where w_n are uniformly distributed in $[-w, w]$. In Fig. 6 we present the dynamics of a Gaussian wave-packet in the presence of a disorder realization with $w = 10^{-7}$, $N = 400$ ($a = 1$). We note that since $\xi \sim 1/w^2 \gg N$ (see Appendix E 1), localization effects will not be observed. Similarly to the reflection case, a transition from the initial wave-packet to another occurs at a certain time. However, in the current case the cause is disorder rather than a wall (here existence of the wall is irrelevant). Also, here the transition happens sooner

than in the no-disorder scenario. The main idea will be introduced here while more technical details are provided in Appendix E.

Examining the wave-packet in k -space, the disorder enables transitions from the center of the wave-packet (initially positioned at k_0) to all other k values. In the case of a Hermitian Hamiltonian, this scattering process continues until it reaches a saturation value determined by the disorder strength w and the system size. However, since the Hamiltonian is non-Hermitian, each k -value also experiences exponential growth or decay. In particular, the most significant k -value which is $k = -\pi/2$ (since it exhibits the fastest growth, as was discussed earlier), will eventually surpass the initial Gaussian wave-packet in magnitude. This explains the transition presented in the figure.

To estimate the transition time, we develop approximations for the amplitudes of both the $k = -\pi/2$ packet and the initial Gaussian wave-packet. We start with the $k = -\pi/2$ packet. Using perturbation theory and averaging over the disorder realizations (denoted by $\langle \rangle$), we find that at small times

$$\langle |c_k(t)|^2 \rangle - |c_k(0)|^2 \approx \frac{t^2}{\hbar^2} \frac{w^2}{3} \frac{1}{N}. \quad (26)$$

At intermediate times this increase saturates, with saturation value and saturation time given approximately by

$$V_s \approx \frac{w^2}{3} \frac{1}{N} \frac{1}{\text{Re}(E_k - E_{k_0})^2}, \quad t_s \approx \frac{\pi}{\text{Re}(E_k - E_{k_0})}, \quad (27)$$

and at later times the non-Hermitian exponential growth sets in:

$$|\psi(k, t)|^2 \approx V_s e^{2(t_l - t_r)(t - t_s)}. \quad (28)$$

Plugging in $k_0 = \frac{\pi}{4}$ and $k = -\pi/2$, yields our first approximation.

For the second approximation, as we observed above, up to intermediate times the Gaussian is well described by the “continuum limit” Hamiltonian. We thus obtain

$$|\psi(k_m, t)|^2 \approx \left(\frac{8\pi\sigma^2}{N^2} \right)^{1/2} e^{2k_0 b t + \frac{b^2}{2\sigma^2} t^2}, \quad (29)$$

where k_m is the maximum of the wave-packet, and $b = \ln\left(\frac{t_r}{t_l}\right) \sqrt{t_l t_r}$. We have verified that both of these approximations are in a very good agreement with the numerical results (see Fig. 12 in Appendix E).

By comparing Eq. (29) and (28), we obtain a quadratic equation, and its solution readily gives the transition time, marked by the green dashed line in Fig. 6. Finally, it is worth noting that even if no disorder is considered ($w = 0$), numerical artifacts may induce such transition. This is because the numerical accuracy of the computer may not be sufficient to capture the evolution of the tail of the wave-packet, effectively introducing a disorder

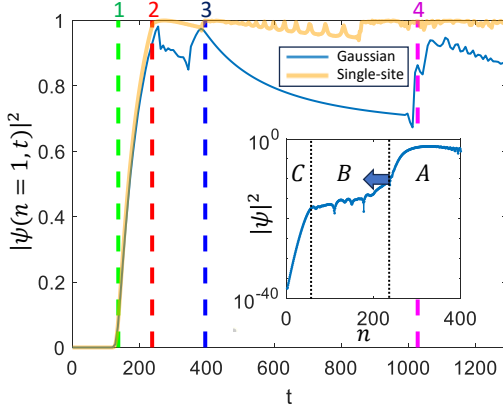


FIG. 7. Blue line: the numerical results of the amplitude at the leftmost site as a function of time, where the initial conditions are the same as in Fig. 6 (a Gaussian with initial position $x_0 = \frac{3N}{2}$). Orange line: the same, but for initial condition $\psi(n, t=0) = \delta_{n,x_0}$ (for $t > t_2$ only the envelope of the wave-packet is shown). We mark the following timestamps (in green, red, blue, and magenta, respectively): $t_1 = \frac{x_0}{v_{nh}}$, $t_2 = \frac{x_0}{v_h}$, $t_3 = \frac{2N-x_0}{v_h}$, $t_4 = \frac{4N-x_0}{4} \frac{1}{v_h}$, where v_h, v_{nh} are the Hermitian and non-Hermitian velocities, given by Eq. (12), (13) respectively. Inset: the Hermitian counterpart of the wave-packet, as a function of n , for $t = 190$ (which is roughly $\frac{t_1+t_2}{2}$). The boundary between regions A and B is given by $2N - x_0 - v_h t$, while the boundary between region B and C is given by $x_0 - v_h t$.

term with amplitude related to the computer precision threshold. To overcome this (for example, to plot the disorder-less scenario that was presented in Fig. 4) one may need to increase the precision by using an arbitrary precision library (such as Advanpix [68] in Matlab).

We can gain more insights by looking at the amplitude of the leftmost site (the left boundary), see Fig. 7. As was demonstrated earlier, for a better understanding of the dynamics it is best to start by examining the behavior of the Hermitian counterpart of the wave-packet: In the inset, we present the Hermitian wave-packet (initially moving to the right) at a time when it has already struck the right wall and now advancing toward the left wall. We highlight three distinct regions: (A) The Gaussian wave-packet itself. (B) The cutoff of the Gaussian caused by disorder: Instead of the expected Gaussian decrease in the absence of disorder, we observe a saturation in the value of $|\psi|^2$. Its specific features depends on the particular disorder realization, while its amplitude is determined by w (see Eq. 27). (C) The tail of the distribution, that is, the wave-packet beyond the maximum Hermitian velocity $x_0 - v_h t$.

We move on to analyzing the non-Hermitian dynamics. In blue we present the result for the Gaussian initial condition (that was discussed here) while for comparison, we add in orange the result for the initial condition δ_{n,x_0} (as was discussed at section III A). We mark four timestamps: the first two, $t_1 = \frac{x_0}{v_{nh}}$, $t_2 = \frac{x_0}{v_h}$, represent

the time that takes for the Hermitian and non-Hermitian wave-packets to reach the boundary, respectively (where the initial expectation value of the distribution is $x_0 = \frac{3N}{4}$). First, we note that up to $t = t_2$, the behavior of the two initial conditions (blue and orange lines) is remarkably similar (see also Fig. 2). This fact implies that the behavior of any (localized) initial condition with some disorder would also look similar up to this time. The reason for this is that in the presence of disorder, the tail of the Hermitian wave-packet (i.e., the wave-packet beyond position $x_0 - v_h t$, corresponding to region C in the Hermitian case) will look similar for any initial distribution, and the tail is the important factor controlling the properties of the non-Hermitian wave-packet.

As for t_2 , this is the time where the disorder-dependent part of the Hermitian wave-packet (that was marked as region B in the inset of Fig. 7) hits the left wall. Then, at $t = t_3$, the front of the Gaussian wave-packet itself (region A) also arrives to the left boundary. Finally, t_4 is the time where the Gaussian wave-packet hits the left boundary for the second time (after being reflected from the other end of the system)[79]. This once again demonstrates that only the Hermitian wave-packets can be reflected.

1. Critical threshold $\sigma_{c,dis}$

The disorder-induced transition discussed above can only be observed when the initial width exceeds a critical value, $\sigma_{c,dis}$, which depends on the disorder strength w . To understand this, it is useful to revisit the wave-packet in quasi-momentum space. As noted earlier, the saturation value of the most significant q is proportional to w^2 , see Eq. (27). However, if σ is sufficiently small in real space, it may be large enough in q -space to surpass this saturation value. When this occurs, the effect of disorder at $q = -\pi/2$ becomes negligible, resulting in a smooth transition. This behavior is illustrated in Fig. 13 in Appendix E. The critical value $\sigma_{c,dis}$ can be explicitly determined by comparing

$$\left| \psi\left(q = -\frac{\pi}{2}\right) \right|^2 = \left(8\pi \frac{\sigma^2}{N^2} \right)^{1/2} e^{-2\frac{\sigma^2}{a^2}(\frac{\pi}{2} + q_0)^2} \quad (30)$$

to the saturation value from Eq. (27) and extracting σ . Finally, we note that for the same reasons, given a fixed value of σ , the transition can only be observed when the disorder exceeds a certain critical value w_c , which depends on σ .

IV. BEYOND THE HATANO-NELSON MODEL

While we have focused on the Hatano-Nelson model for simplicity, most of the discussion above—specifically the coexistence of Hermitian and non-Hermitian wave-packets—should also apply to more complex models,

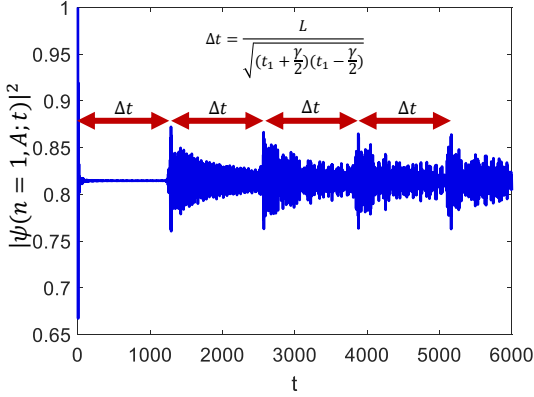


FIG. 8. Numerical calculation of the amplitude at the leftmost site as a function of time, for the non-Hermitian SSH model in Eq. (31). The parameters are $t_1 = 0.4$, $t_2 = 1$, $\gamma = 0.5$. The wavefunction is initially localized at the leftmost site. The time difference between each peak is given by $\Delta t = 2L/v_h$, where $v_h = 2\sqrt{(t_1 + \gamma/2)(t_1 - \gamma/2)}$ is the velocity of the Hermitian wave-packet.

provided that the Hamiltonian is pseudo-Hermitian. For example, we will now focus on a specific version of the non-Hermitian SSH model [41, 65]. We consider the Hamiltonian

$$H = \sum_n \left(t_1 - \frac{\gamma}{2} \right) |n, A\rangle \langle n, B| + \left(t_1 + \frac{\gamma}{2} \right) |n, B\rangle \langle n, A| + (t_2 |n, B\rangle \langle n+1, A| + h.c.) , \quad (31)$$

which is pseudo-Hermitian, as it can become Hermitian using the transformation $H' = S^{-1}HS$ where

$$S = |1, A\rangle \langle 1, A| + r^N |N, B\rangle \langle N, B| + \sum_{n=1}^{N-1} [r^n |n, B\rangle \langle n, B| + r^n |n+1, A\rangle \langle n+1, A|] \quad (32)$$

(that is, the diagonal components are $1, r, r^2, r^3, \dots, r^{N-1}, r^N$, where $r = \sqrt{(t_1 + \gamma/2)/(t_1 - \gamma/2)}$). We emphasize again that the discussion in Sec. II remains valid, meaning that we anticipate the coexistence of Hermitian and non-Hermitian wave-packets in this setup as well. Consider, for example, the configuration in Fig. 8, which illustrates the dynamics of the leftmost site. Initially, the wavefunction is localized at $n = 1$, but as it evolves, the Hermitian component of the wave-packet propagates to the other edge of the system and gets reflected back. Hence, we observe oscillations with a period of $\Delta t = 2L/v_h$, where $v_h = 2a \min(\tilde{t}_1, t_2)$ is the velocity of the Hermitian SSH model and $\tilde{t}_1 = \sqrt{(t_1 + \gamma/2)(t_1 - \gamma/2)}$ is the effective hopping amplitude after the transformation. Notably, the saturation of the average amplitude at approximately 0.8 suggests the presence of a topological edge state,

indicating that classifying the topological phase based on dynamics may be possible. We plan to examine this in more detail in future work. Finally, we note that in principle, all of the other phenomena discussed in Sec. III can also be observed in this setup, but in practice some of them would be more elusive. We elaborate on this in Appendix F.

V. DISCUSSION AND CONCLUSIONS

In this paper we explored the dynamics of pseudo-Hermitian systems, highlighting the unexpected coexistence of Hermitian and non-Hermitian wave-packets. Focusing primarily on the Hatano-Nelson model with open boundary conditions, we demonstrated that the two dynamics are interconnected through a local transformation. Importantly, we show that the Hermitian wave-packet is not merely a mathematical abstraction; it exists within the system, propagates, and can reflect off boundaries. This is evident even in the simplest case of a single-site initial condition (i.e., when the width $\sigma \ll a$), where oscillations near the boundaries occur with a period matching the time taken for the Hermitian wave-packet to travel to the opposite end and return.

For moderate widths (i.e., $a < \sigma \ll L$), we showed that the coexistence of these wave-packets is essential for explaining more complex phenomena, such as non-Hermitian reflection at the boundary. The transition occurs when the Hermitian wave-packet hits the wall (although it may not be observed until some time later due to lattice effects). Notably, the non-Hermitian wave-packet does not need to be close to the wall during the transition, reinforcing the idea that the Hermitian wave-packet is the crucial element in the reflection process. Additionally, we revealed that the transition due to disorder, typically attributed to the amplification of certain k -values, can also be interpreted as the tail of the Hermitian wave-packet becoming dominant over time due to the exponential transformation connecting the two dynamics. Finally, we examine a version of the non-Hermitian SSH model to demonstrate that our results generalize to pseudo-Hermitian models beyond just the Hatano-Nelson model. We believe that this new perspective on the dynamics can significantly enhance the understanding of pseudo-Hermitian systems.

A pertinent question arises: Can the tool of investigate the dynamics using a transformation remain effective when the Hamiltonian is not pseudo-Hermitian? Preliminary results for simpler models, such as the Hatano-Nelson model with complex coefficients, suggest that this approach is still beneficial. By applying a transformation, we can attain a Hamiltonian that, while not being Hermitian, does not favor one direction (i.e., $|t_l| = |t_r|$), which can simplify the analysis. However, for more complex models, such as the general non-Hermitian SSH model, it remains unclear to what extent

the methodology developed here will apply. Future research will delve deeper into cases beyond the pseudo-Hermitian framework.

Another promising direction for investigation is to leverage the tools derived here to explore the topology of pseudo-Hermitian systems and classify it based on their dynamics. For this, we can consider pseudo-Hermitian topological models such as the non-Hermitian SSH model discussed in Sec. IV. These tools can assist in investigating how non-Hermitian effects influence topological properties, particularly the stability and behavior of edge states.

Note added. After completing this work we have become aware of the very recent preprint by He and Ozawa (Ref. [80]) on wave-packet dynamics in the Hatano-Nelson model, reporting a similar boundary-associated non-Hermitian reflection (jump). However, their analysis emphasizes the point of view of temporal Goos-Hänchen shifts at the edge, while we uncover the coexistence of the Hermitian and non-Hermitian wavefronts as the basis for this phenomenon.

ACKNOWLEDGMENTS

We would like to thank Guy Gabrieli for unpublished results which motivated this study. Our work has been supported by the Israel Science Foundation (ISF) and the Directorate for Defense Research and Development (DDR&D) Grant No. 3427/21, the ISF Grant No. 1113/23, and the US-Israel Binational Science Foundation (BSF) Grants No. 2020072 and 2024140.

Appendix A: Hermitian dynamics of a Gaussian wave-packet

Suppose we have a Gaussian wave-packet, given by

$$|\psi(t=0)\rangle = N \sum_n e^{-\frac{n^2 a^2}{4\sigma^2} + i k_0 a n} |n\rangle, \quad (\text{A1})$$

where $N \approx (2\pi\sigma^2/a^2)^{-\frac{1}{4}}$. We will now compute $\psi(m, t) = \langle m | e^{-iHt} | \psi(0) \rangle$, where the Hermitian Hamiltonian is given by

$$H = t_0 \sum_n |n\rangle \langle n+1| + h.c. \quad (\text{A2})$$

We first notice that the expression can be written as the discrete convolution of ψ and the propagator, that is

$$\psi(m, t) = \sum_n g(m-n, t) \psi_0(n), \quad (\text{A3})$$

where we have defined $g(m-n, t) \equiv \langle m | e^{-iH't} | n \rangle$ (due to discrete translational invariance g is only a function of only the difference $m-n$, see Eq. (10)) and

$$\psi_0(n) \equiv \langle n | \psi(0) \rangle = N e^{-\frac{n^2 a^2}{4\sigma^2} + i k_0 a n}. \quad (\text{A4})$$

For large N , we can use discrete Fourier transform. For any function $f : \mathbb{N} \rightarrow \mathbb{R}$ we can define $F : (-\pi, \pi) \rightarrow \mathbb{R}$ by the relations

$$f(n) = \frac{1}{2\pi} \int_{-\pi}^{\pi} F(q) e^{iqn} dq, \quad F(q) = \sum_{n=-\infty}^{\infty} f(n) e^{-iqn}, \quad (\text{A5})$$

where we define $q = ka$. Taking the limits of the sum in Eq. (A3) to infinity, and using the convolution theorem, we get that

$$\Psi(q, t) = G(q, t) \Psi_0(q), \quad (\text{A6})$$

where $\Psi(q, t), G(q, t), \Psi_0(q)$ are the discrete Fourier transform of $\psi(n, t), g(n, t), \psi_0(n)$, respectively, and we note that $G(q, t) = e^{-2it_0 \cos(q)t}$. We can calculate $\Psi_0(q)$ explicitly: Employing the fact that

$$\sqrt{\frac{\pi}{\sigma^2}} e^{-\frac{n^2}{4\sigma^2}} = \int_{-\infty}^{\infty} e^{-inx} e^{-\sigma^2 x^2} dx, \quad (\text{A7})$$

and using the Poisson summation formula

$$\frac{1}{2\pi} \sum_n e^{int} = \sum_m \delta(t - 2\pi T), \quad (\text{A8})$$

we obtain

$$\Psi_0(q) = \sum_m e^{-\frac{\sigma^2}{a^2}(q-q_0-2\pi m)^2}. \quad (\text{A9})$$

Assuming also that $\sigma \gtrsim a$ (and $|q_0| \leq \pi/2$), the only significant contribution comes from $m = 0$ so we are left with $\Psi_0(q) = e^{-\frac{\sigma^2}{a^2}(q-q_0)^2}$. Performing the inverse transform on Eq. (A6), we get

$$\psi(m, t) = N_q \int_{-\pi}^{\pi} e^{-\frac{\sigma^2}{a^2}(q-q_0)^2} e^{-2it_0 \cos(q)t} e^{iqm} dq, \quad (\text{A10})$$

$$N_q = \frac{(8\pi\sigma^2/a^2)^{1/4}}{2\pi}. \quad (\text{A11})$$

To proceed, it will be convenient to define a “velocity” $v(m, t)$ by $vt \equiv am$. Then, we can rewrite Eq. (A10) as

$$\psi(v, t) = N_q \int_{-\pi}^{\pi} e^{-\frac{\sigma^2}{a^2}(q-q_0)^2} e^{i\frac{tv_{\max}}{a} A(q, v)} dq, \quad (\text{A12})$$

where we have defined

$$A(q, v) \equiv \frac{v}{v_{\max}} q - \cos(q). \quad (\text{A13})$$

For $t \gg 1/t_0$, this integral can be evaluated by the stationary phase approximation:

$$\begin{aligned} \psi(v, t) \approx N_q \sum_j & e^{i\frac{tv_{\max}}{a} A(q_j, v)} e^{-\frac{\sigma^2}{a^2}(q_j-q_0)^2} \times \\ & \times \sqrt{\frac{2\pi}{\frac{tv_{\max}}{a} \left| \frac{\partial^2}{\partial^2 q} A(q_j, v) \right|}} e^{\text{sign}\left(\frac{\partial^2}{\partial^2 q} A(q_j, v)\right) \frac{i\pi}{4}}, \end{aligned}$$

where the sum \sum_j is over all of the q_j satisfying

$$\frac{\partial}{\partial q} A(q_j) = \frac{v}{v_{\max}} + \sin(q) = 0. \quad (\text{A14})$$

We will now note that for $|v| < v_{\max}$ the solution is real, and complex otherwise. We will start with the case of $|v| < v_{\max}$ (where $v_{\max} \equiv 2at_0$, as the Hermitian maximal velocity v_h in the main text). In this case we obtain two solutions

$$q_1 = \arcsin(-v/v_{\max}), \quad q_2 = \pi - q_1, \quad (\text{A15})$$

and therefore

$$A(q_{1,2}, v) \equiv \frac{v}{v_{\max}} q_{1,2} \mp \sqrt{1 - (v/v_{\max})^2}, \quad (\text{A16})$$

$$\frac{\partial^2}{\partial^2 q} A(q_j, v) = \pm \sqrt{1 - (v/v_{\max})^2}. \quad (\text{A17})$$

Without loss of generality, we assume that $|q_1 - q_0| < |q_2 - q_0|$ so that $e^{-\frac{\sigma^2}{a^2}(q_1 - q_0)^2} \ll e^{-\frac{\sigma^2}{a^2}(q_2 - q_0)^2}$ (since $\sigma \gtrsim a$), so we can keep only the first term and finally arrive at

$$\psi(m, t) \approx \frac{(8\pi\sigma^2/a^2)^{1/4}}{\sqrt{2\pi}} e^{\frac{i\pi}{4}} e^{i\frac{tv_{\max}}{a} A} \frac{e^{-\frac{\sigma^2}{a^2}(\arcsin(-\frac{am}{tv_{\max}}) - q_0)^2}}{\sqrt{\frac{t}{a}v_{\max} \sqrt{1 - \left(\frac{am}{tv_{\max}}\right)^2}}}, \quad (\text{A18})$$

where

$$A = \frac{v}{v_{\max}} \arcsin\left(-\frac{am}{tv_{\max}}\right) - \sqrt{1 - \left(\frac{am}{tv_{\max}}\right)^2}. \quad (\text{A19})$$

A comparison of this result to numerical results is shown in Fig. 9.

Except for when $am \approx tv_{\max}$, we may do one more simplification by setting $\arcsin(-v/v_{\max}) = q_0$ outside of the exponent. Taking also the absolute value and switching back to m, k , we finally get

$$\psi(m, t) \approx \frac{(8\pi\sigma^2/a^2)^{1/4}}{\sqrt{2\pi\frac{t}{a}v_{\max} \cos(ak_0)}} \times e^{\frac{i\pi}{4}} e^{i\frac{tv_{\max}}{a} A} e^{-\frac{\sigma^2}{a^2}(\arcsin(-\frac{am}{tv_{\max}}) - ak_0)^2}. \quad (\text{A20})$$

One can check that for $a \rightarrow 0$ this results approaches the known result in continuum (a Gaussian wave-packet moving at a constant velocity while becoming broader).

As was shown in Fig. 9, the results for the case $|v| < v_{\max}$ provide an excellent approximation for the Hermitian wave-packet when the time is sufficiently large. However, it is important to note that for non-Hermitian wave-packets in the long-time limit, the behavior is primarily governed by the tail of the distribution, where the approximation breaks down. This implies that,

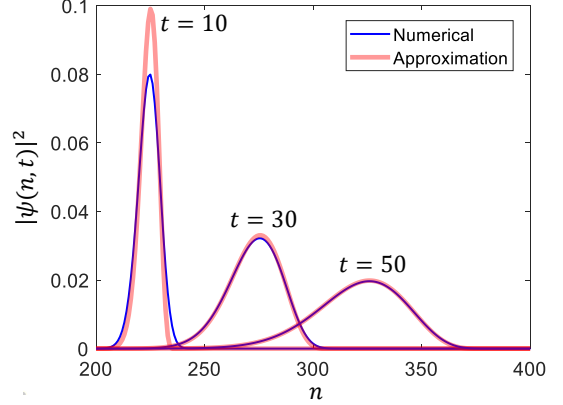


FIG. 9. Numerical calculation of $e^{-iHt} |\psi_0\rangle$, where H is given by Eq. (A2) and ψ_0 is the Gaussian given by Eq. (A1), versus the approximation given by Eq. (A18), at times $t = 10, 30, 50$. As t grows, the Gaussian wave-packet acquires a non-symmetrical shape, due to the fact that the maximum velocity on the lattice is finite. The parameters are $n_0 = 200$, $\sigma = 3$, $a = 1$, $k_0 = \pi/4$, and $t_0 = \sqrt{3}$. See Video_6 in the Supplemental Material for an animation of the dynamics.

for accurate long-time approximations, considering the $|v| > v_{\max}$ case may also be necessary. Although for most phenomena presented in this paper this additional consideration is not essential, for completeness, we will also derive the approximation for $|v| > v_{\max}$. We are looking for the solutions of $\frac{v}{v_{\max}} + \sin(q) = 0$, which will now be on the complex plane (and therefore we can use the method of steepest decent). Plugging $q = q' + iq''$, we are looking for the solutions of

$$\frac{v}{v_{\max}} + \sin(q') \cosh(q'') + i \sinh(q'') \cos(q') = 0. \quad (\text{A21})$$

Since $q'' = 0$ will not yield a solution for $|v| > v_{\max}$, we take $q'' \neq 0$ and get

$$q' = -\text{sign}(v)\frac{\pi}{2}, \quad q'' = -\text{sign}(v)\text{arccosh}\left(\frac{|v|}{v_{\max}}\right), \quad (\text{A22})$$

where we chose the sign of q'' so that the critical point would be a maximum, on a contour that passes through it with fixed $q' = -\text{sign}(v)\frac{\pi}{2}$ (that is, on this contour the imaginary part in the argument of the exponent is constant). Then, we can use the saddle point approximation to find

$$\begin{aligned} \psi(m, t) = & \sqrt{2\pi} N_q e^{-i\frac{tv}{a}\text{sign}(m)\frac{\pi}{2}} \times \\ & e^{i\frac{\sigma^2}{a^2}2(-\text{sign}(m)\frac{\pi}{2}-q_0)\text{sign}(m)\text{arccosh}\left(\frac{|m|a}{v_{\max}t}\right)} \times \\ & e^{\frac{\sigma^2}{a^2}[\text{arccosh}^2\left(\frac{|m|a}{v_{\max}t}\right) - (-\text{sign}(m)\frac{\pi}{2}-q_0)^2]} \times \\ & \frac{e^{-|m|\text{arccosh}\left(\frac{|m|a}{v_{\max}t}\right) + \frac{tv_{\max}}{a}\sqrt{m^2 - \frac{t^2 v_{\max}^2}{a^2}}}}{\sqrt{m^2 - \frac{t^2 v_{\max}^2}{a^2}}}. \end{aligned}$$

Appendix B: Small t expansion for Eq. (18)

As described by Eq. (18) in the main text, the evolved Gaussian wave-packet governed by the non-Hermitian counterpart is approximately equal to

$$\langle m | e^{-iHt} | \psi(0) \rangle \approx \tilde{C} r^m e^{-\frac{\sigma^2}{a^2} \left(\arcsin\left(\frac{am}{tv_h}\right) - ak_0 \right)^2}, \quad (\text{B1})$$

where \tilde{C} is some constant, and we assume that $\tilde{n}_0 = 0$ for convenience. As shown in Fig. 3 in the main text, this approximation is in a good agreement with the numerical results except for two discrepancies. The first one is just a small shift of $\frac{2\sigma^2}{a^2} \ln r$ in its initial position (see Eq. (16)), which is due to the fact that at $t = 0$ the approximation is localized at a certain position (since it has no width, the transformation r^m cannot move its center ‘‘back’’). The second one is just the fact that the velocity of the approximation does saturates to v_h instead of v_{nh} , as discussed in the main text.

We begin by finding the peak of $|\langle m | e^{-iHt} | \psi(0) \rangle|^2$ by maximizing the parameter of the exponent. That is, m_{\max} is obtained from a solution of the equation

$$2(\sigma/a)^2 \left(\arcsin\left(\frac{a}{tv_h} m\right) - ak_0 \right) \frac{\frac{a}{tv_h}}{\sqrt{1 - \left(\frac{am}{tv_h}\right)^2}} = \ln(r). \quad (\text{B2})$$

We now investigate this equation for $\frac{tv_h}{a} \ll 1$.

First, we re-write this expression as a self-consistent equation

$$m_{\max} = \frac{tv_h}{a} \sin(ak_0 + \Delta(m_{\max})), \quad (\text{B3})$$

where Δ is a function of m defined by

$$\Delta(m_{\max}) \equiv \frac{1}{2(\sigma/a)^2} \frac{tv_h}{a} \ln(r) \sqrt{1 - \left(\frac{a}{tv_h} m_{\max}\right)^2}. \quad (\text{B4})$$

We can solve this equation iteratively, order by order, in $\frac{tv_h}{a}$. The first order is just given by

$$m_1 = \sin(ak_0) \frac{tv_h}{a}. \quad (\text{B5})$$

Recalling that $\sin(ak_0 + \Delta) \approx \sin(ak_0) + \Delta \cos(ak_0) - \frac{1}{2} \Delta^2 \sin(ak_0)$, we see that the second order is given by

$$m_2 = \frac{1}{2(\sigma/a)^2} \cos^2(ak_0) \ln(r) \left(\frac{tv_h}{a}\right)^2. \quad (\text{B6})$$

The third order ($\propto (\frac{tv_h}{a})^3$) will be obtained as the sum of two terms:

$$m_3 = m_{3,A} + m_{3,B}, \quad (\text{B7})$$

where the first term $m_{3,A}$ is $(\frac{tv_h}{a}) \Delta_2 \cos(ak_0)$, where $\Delta_2 \propto (\frac{tv_h}{a})^2$ is the second order term in the expansion

of Δ in powers of $\frac{tv_h}{a}$, and the second term $m_{3,B}$ comes from the second order of the Taylor expansion, $-(\frac{tv_h}{a}) \frac{1}{2} \Delta_1^2 \sin(ak_0)$, where $\Delta_1 \propto (\frac{tv_h}{a})$ is the first order. A short calculation leads to

$$m_{3,A} = 2m_{3,B} = -\frac{1}{4(\sigma/a)^4} \cos^2(ak_0) \sin(ak_0) \ln^2(r) \left(\frac{tv_h}{a}\right)^3,$$

and therefore we have

$$m_3 = -\frac{3}{8(\sigma/a)^4} \cos^2(ak_0) \sin(ak_0) \ln^2(r) \left(\frac{tv_h}{a}\right)^3. \quad (\text{B8})$$

Appendix C: The continuum limit of the Hatano-Nelson model

We start with the Hamiltonian

$$H_0 = \sum_{n=1}^{N_0} t_{l,0} |na_0\rangle \langle na_0 + a_0| + t_{r,0} |na_0 + a_0\rangle \langle na_0|, \quad (\text{C1})$$

where a_0 is the lattice spacing (initially, before taking the continuum limit), and the total system size is $L = N_0 a_0$. We recall that the transformation (6) will make the Hamiltonian Hermitian, where $r_0 = \left(\frac{t_{r,0}}{t_{l,0}}\right)^{1/2}$. We will now consider the continuum limit by taking $x = na$, where $a \rightarrow 0$ (and $n \rightarrow \infty$ for any finite x). Since we expect that after the transformation $r^n \psi(na)$ will converge (for $a \rightarrow 0$) to a finite limit only as a function of $x = na$, then we can write $r_0^{n_0} = r^n$ where $n_0 a_0 = na$, and therefore

$$r = \left(\frac{t_{r,0}}{t_{l,0}}\right)^{a/2a_0}. \quad (\text{C2})$$

We now take

$$t_l = \frac{1}{r} \sqrt{t_l t_r} \approx \sqrt{t_l t_r} \left(1 - \frac{a}{2a_0} \ln\left(\frac{t_{r,0}}{t_{l,0}}\right)\right), \quad (\text{C3})$$

$$t_r = r \sqrt{t_r t_l} \approx \sqrt{t_l t_r} \left(1 + \frac{a}{2a_0} \ln\left(\frac{t_{r,0}}{t_{l,0}}\right)\right), \quad (\text{C4})$$

where the approximation is valid for $a \rightarrow 0$. Now, we define as usual $|x\rangle \equiv \frac{1}{\sqrt{a}} |na\rangle$ and transform the sum into integral, resulting in

$$H = \int_0^L [t_l |x\rangle \langle x + a| + t_r |x + a\rangle \langle x|] dx. \quad (\text{C5})$$

Approximating $|x + a\rangle \approx |x\rangle + a\partial_x |x\rangle + \frac{a^2}{2} \partial_x^2 |x\rangle$ and assuming periodic boundary conditions, we get that

$$H = H_h + H_{nh}, \quad (\text{C6})$$

where H_h, H_{nh} , the Hermitian and non-Hermitian parts, are given by

$$H_h = \sqrt{t_l t_r} \int_0^L (2|x\rangle\langle x| - a^2|x\rangle\partial_x^2\langle x|), \quad (\text{C7})$$

$$H_{nh} = \frac{a}{a_0} \ln\left(\frac{t_{r,0}}{t_{l,0}}\right) \sqrt{t_l t_r} \int_0^L |x\rangle\partial_x\langle x|. \quad (\text{C8})$$

Therefore, the continuum Hamiltonian is given by

$$H = E_0 - \frac{1}{2m}\partial_x^2 + b\partial_x, \quad (\text{C9})$$

where $E_0 = 2\sqrt{t_l t_r}$, $m = 1/(2a^2\sqrt{t_l t_r})$, and $b = \frac{a^2}{a_0} \ln\left(\frac{t_{r,0}}{t_{l,0}}\right) \sqrt{t_l t_r}$. Since m, b should be finite, while taking the limit $a \rightarrow 0$ we need to keep

$$\sqrt{t_l t_r} = \frac{a_0^2}{a^2} \sqrt{t_{l,0} t_{r,0}}, \quad (\text{C10})$$

and therefore we finally get

$$m = \frac{1}{2a_0^2 \sqrt{t_{l,0} t_{r,0}}}, b = a_0 \ln\left(\frac{t_{r,0}}{t_{l,0}}\right) \sqrt{t_{l,0} t_{r,0}}. \quad (\text{C11})$$

Appendix D: Calculation of the transition time of the non-Hermitian reflection

In Section III B 2 we showed that in the presence of a wall, the wave-packet could experience a sudden change in its behavior, related to the reflection event of the Hermitian wave-packet. Here, we will show that in the continuum limit, the time of this event (i.e., the time when the non-Hermitian wave-packet changes its velocity), is completely determined by t_{hit} , the time that it takes to the *Hermitian* wave-packet to hit the wall. On the lattice, however, the time is larger than t_{hit} . We will also calculate here the first correction to this time in orders of a , the lattice spacing.

We will start by using our approximation (Eq. A20), to write the wave-packet as

$$|\langle m|\psi(t)\rangle|^2 \approx e^{-2\frac{\sigma^2}{a^2}(\arcsin\left(\frac{am}{tv_h}\right) - ak_0)^2 + 2m\ln(r)}, \quad (\text{D1})$$

where we assume that the center at $t = 0$ is $m = 0$. We are interested in the amplitude of this expression at the peak point, m_{max} . Using Eq. (B2), we see that

$$2(\sigma/a)^2 \left(\arcsin\left(\frac{a}{tv_h}m_{\text{max}}\right) - ak_0 \right) = \frac{\sqrt{1 - \left(\frac{am_{\text{max}}}{tv_h}\right)^2}}{\frac{a}{tv_h}} \ln(r),$$

and therefore we get

$$|\langle m_{\text{max}}|\psi(t)\rangle|^2 \approx e^{-\frac{\sqrt{1 - \left(\frac{am_{\text{max}}}{tv_h}\right)^2}}{\frac{a}{tv_h}} \ln(r) + 2m_{\text{max}}\ln(r)}. \quad (\text{D2})$$

Since we assumed that the lattice spacing is small, the transition must occur at small times as well. Thus, we write $m_{\text{max}}(t) \approx \sin(ak_0)\frac{tv_h}{a}$ and therefore $\frac{\sqrt{1 - \left(\frac{am_{\text{max}}}{tv_h}\right)^2}}{\frac{a}{tv_h}} = 2t \cos(ak_0)\sqrt{t_r t_l} \approx 0$, so we get that $|\langle m_{\text{max}}|\psi(t)\rangle|^2 \approx e^{2m_{\text{max}}(t)\ln(r)}$. Since the amplitude of the peak is given by the exponent of m_{max} , the time at which the amplitude of the image wave-packet surpasses that of the incident wave-packet (and therefore becomes more dominant) is the time when the maximum position m_{max} of the former surpasses that of the latter. Therefore, we will write m_{max} for both wave-packets and set them equal.

We can expand m_{max} for small times as

$$\Delta m_{\text{max}}(t, k_0) \approx A(k_0)t + B(k_0)t^2 + C(k_0)t^3, \quad (\text{D3})$$

where $\Delta m_{\text{max}}(t, k_0) = m_{\text{max}}(t, k_0) - m_0$, and the coefficients are, respectively (see Appendix B),

$$\begin{aligned} A(k_0) &= \sin(ak_0)\frac{v_h}{a}, \\ B(k_0) &= \frac{\ln(r)}{2(\sigma/a)^2} \cos^2(ak_0) \left(\frac{v_h}{a}\right)^2, \\ C(k_0) &= -\frac{3\ln^2(r)}{8(\sigma/a)^4} \cos^2(ak_0) \sin(ak_0) \left(\frac{v_h}{a}\right)^3. \end{aligned}$$

We note that A, C are odd in k_0 , while B is even. Assuming that the initial distance from the wall is d , the maximum position of the incident and the image wave-packet are respectively given by

$$m_{\text{max}}^{\text{inc}}(t) = -\frac{d}{a} + \Delta m_{\text{max}}(t, k_0), \quad (\text{D4})$$

$$m_{\text{max}}^{\text{img}}(t) = \frac{d}{a} + \Delta m_{\text{max}}(t, -k_0). \quad (\text{D5})$$

We wish to find the transition time t where these expressions become equal. Comparing them we find

$$\Delta m_{\text{max}}(t, k_0) - \Delta m_{\text{max}}(t, -k_0) = 2\frac{d}{a}, \quad (\text{D6})$$

which leads to

$$A(k_0)t + C(k_0)t^3 = \frac{d}{a}. \quad (\text{D7})$$

For small lattice spacing $C(k_0)$ will be small in comparison to $A(k_0)$, and we get to first order that

$$t_{\text{hit}} = \frac{d/a}{A(k_0)} = \frac{d}{\sin(ak_0)v_h}. \quad (\text{D8})$$

This is exactly the time it takes to the Hermitian wave-packet to hit the wall, as expected. Plugging $t = t_{\text{hit}} + t_\delta$ into Eq. (D7) where t_δ is the difference from the Hermitian transition time, we find that the leading order in a is

$$t_\delta \approx \frac{t_{\text{hit}}^3}{-A(k_0)/C(k_0)}. \quad (\text{D9})$$

Keeping a_0 to be some reference lattice constant (where $a \ll a_0$), we have $v_h = 2a\sqrt{t_l t_r}$ where $\sqrt{t_l t_r} = \frac{a_0^2}{a^2} \sqrt{t_{l,0} t_{r,0}}$, and $r = \left(\frac{t_{r,0}}{t_{l,0}}\right)^{a/2a_0}$ (see Appendix C). Plugging this into Eq. (D8,D9), we finally obtain

$$t_{\text{hit}} = \frac{d}{\frac{\sin(ak_0)}{a} a_0^2 \sqrt{t_{l,0} t_{r,0}}}, \quad (\text{D10})$$

$$t_\delta \approx \frac{3}{64} \frac{\ln^2\left(\frac{t_{r,0}}{t_{l,0}}\right)}{\sqrt{t_{l,0} t_{r,0}}} \frac{\cos^2(ak_0)}{\frac{\sin(ak_0)^3}{a^3}} \frac{d^3 a^2}{a_0^4 \sigma^4}. \quad (\text{D11})$$

1. The effects of σ and d on the transition

As described in the main text, the width σ and the initial distance from the wall d have a significant effect on whether the transition will occur (i.e., whether the image wave-packet becomes more dominant than the original wave-packet). In Fig. 10, we present the dynamics for three values of σ . We observe that $\sigma = 2.5$ and $\sigma = 2$ are above the critical threshold (a transition is visible), while $\sigma = 1.5$ is below it. The reason for this can be identified in the bottom panels of the figure, where we plot the amplitude of the peaks of the original and image wave-packets. The intersection point represents the time when the image wave-packet becomes more dominant than the original wave, and thus, a transition is observed. We can see that reducing σ causes the acceleration toward the limiting velocity (which corresponds to the growth rate) to increase, until at some point the intersection no longer occurs. In Fig. 11, we observe a similar effect when σ is held constant, but the distance d from the wall is varied. We see that the critical value of σ depends on d .

To determine this critical value, we can use the approximation derived above. The peak position can be found by solving Eq. (B2), and the amplitude can be obtained by substituting this result into Eq. (B1). We can then calculate the growth of both the real and image waves, noting that the initial amplitude of the image wave-packet is lower by a factor of r^{2d} , and that its initial momentum is $-k_0$ rather than k_0 . Finally, we can check the minimum value of σ for which such an intersection occurs.

Appendix E: Effect of disorder: Supplemental details

1. Localization length estimation

In Section III C we discussed the effect of disorder, by considering an onsite disorder term $\sum_n w_n |n\rangle \langle n|$, where w_n are uniformly distributed in $[-w, w]$. Here, we will provide a simple estimation for the localization length as a function of w and show that $\xi \propto W^{-2}$. Therefore, for the value that were chosen in Section III C ($L = 400a$, $w = 10^{-7}$), we get that $\xi \gg L$ indicating that the disorder is weak and does not lead to localization. Starting from the Fermi's golden rule for a time-independent potential, we have

$$\frac{1}{\tau_{i \rightarrow f}} = 2\pi |\langle f | V | i \rangle|^2 \rho(E_f) \delta(E_f - E_i), \quad (\text{E1})$$

where $\tau_{i \rightarrow f}$ is the scattering time between states i, f . Taking $|i, f\rangle = \frac{1}{\sqrt{N}} \sum_n e^{ik_{i,f} n} |n\rangle$ and $\langle n' | V | n \rangle = V(n) \delta_{n,n'}$, we get

$$|\langle f | V | i \rangle|^2 = \frac{1}{N^2} \sum_{n,n'} e^{i(k_i - k_f)(n - n')} V(n) V(n'). \quad (\text{E2})$$

Denoting the average over disorder realizations by $\langle \rangle$, we get that $\langle V(n) V(n')^* \rangle = \frac{w^2}{3} \delta_{n,n'}$, since $V(n)$ which is independent and uniformly distributed over the interval $[-w, w]$. Therefore, we get $\langle |\langle f | V | i \rangle|^2 \rangle = \frac{1}{N} \frac{w^2}{3}$, so the total scattering time is $\frac{1}{\tau} = \int dE_f \frac{1}{\tau_{i \rightarrow f}} = 2\pi \frac{1}{N} \frac{w^2}{3} \rho(E)$. Plugging the density of states on the 1D lattice $\rho(E) = \frac{N}{2\pi t_0} \frac{1}{\sqrt{1 - \frac{E^2}{4t_0^2}}}$, we find that

$$\frac{1}{\tau} = \frac{w^2}{3} \frac{1}{t_0} \frac{1}{\sqrt{1 - \frac{E^2}{4t_0^2}}}. \quad (\text{E3})$$

We also note that the velocity on the lattice is $v = \frac{\partial E}{\partial k} = 2at_0 \sqrt{1 - \frac{E^2}{4t_0^2}}$. Finally, since in 1D the localization length ξ is just the mean free path, we get that

$$\xi(E) = \tau v = 6a \frac{t_0^2}{w^2} \left(1 - \frac{E^2}{4t_0^2}\right). \quad (\text{E4})$$

2. Analysis of disorder effects and calculation of the transition time

In this section we will analyze the dynamics of a Gaussian wave-packet with disorder. We will also estimate the transition time, which is the time the wave-packet's peak change its position due to disorder, as presented in Fig. 6. Again, we consider the Hamiltonian $H = H_0 + H'$, where H_0 is given by Eq. (3), and the disorder term is given by $H' = \sum_n w_n |n\rangle \langle n|$, where w_n

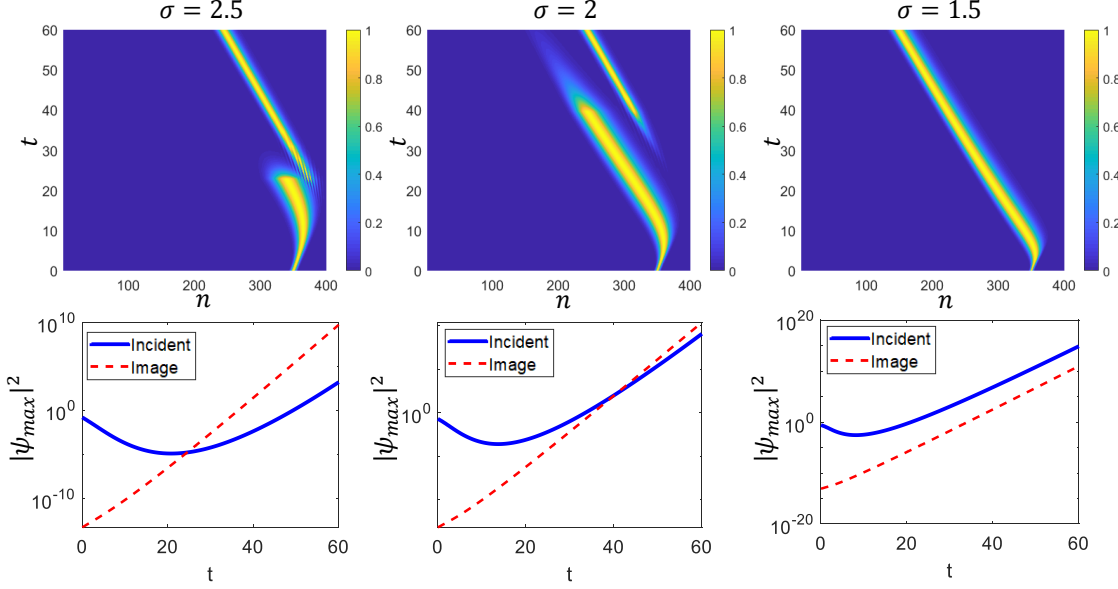


FIG. 10. Top panels: the dynamics of the non-Hermitian wavepacket, with parameters identical to those of Fig. 4, but with initial distance from the wall $d = 50$ (instead of 100), and for three different values of the initial widths $\sigma = 2.5, 2, 1.5$. Bottom panels: The amplitude of the peak of the Gaussian, for the incident wave-packet (in blue) and its image (red dotted-line). We can see that $1.5 < \sigma_{c,\text{ref}} < 2$.

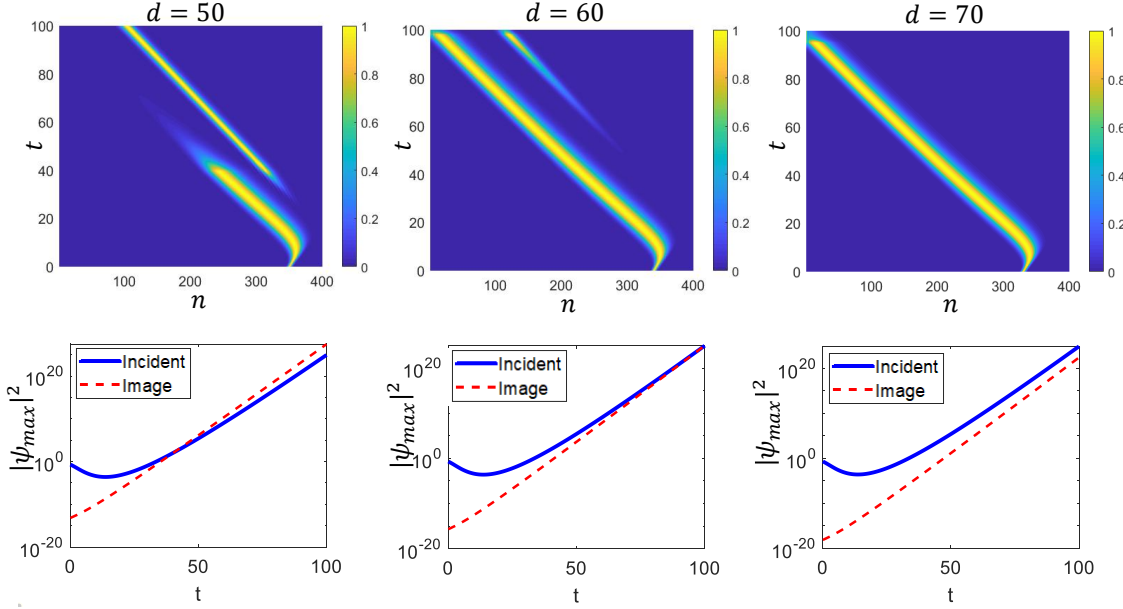


FIG. 11. Top panels: the dynamics of the non-Hermitian wavepacket, with parameters identical to those of Fig. 4, but with $\sigma = 2$, and for three different values of initial distance from the wall, $d = 50, 60, 70$. Bottom panels: The amplitude of the peak of the Gaussian, for the incident wave-packet (in blue) and its image (red dotted-line).

are uniformly distributed in $[-w, w]$. Any wave-function can be written as

$$|\psi(t)\rangle = \sum_k c_k(t) e^{-iE_k t} |k\rangle, \quad (\text{E5})$$

where $|k\rangle$ is the eigenbasis of H_0 ($H_0 |k\rangle = E_k |k\rangle$), $c_k(t = 0) = \langle k| \psi(t = 0) \rangle$, and $e^{-iE_k t}$ is the dynamic

phase factor. Thus, we see that

$$\begin{aligned} \frac{\partial c_k(t)}{\partial t} + \frac{i}{\hbar} \langle k | H' | k \rangle c_k(t) = \\ - \frac{i}{\hbar} \sum_{k' \neq k} c_{k'}(t) e^{-it(E_k - E_{k'})/\hbar} \langle k | H' | k' \rangle. \end{aligned}$$

Multiplying by the integration factor $e^{\frac{i}{\hbar} \langle k | H' | k \rangle t}$ and taking the integral, we get

$$\begin{aligned} e^{\frac{i}{\hbar} \langle k | H' | k \rangle t} c_k(t) = \\ c_k(0) - \int_0^t \frac{i}{\hbar} \sum_{k' \neq k} c_{k'}(t=0) e^{-\frac{i}{\hbar} t(E_k - E_{k'} - \langle k | H' | k \rangle)} \langle k | H' | k' \rangle. \end{aligned}$$

To obtain the first-order behavior for small t , we assume that $c_k(t) = c_k(t=0)$ in the sum and find

$$\begin{aligned} c_k(t) = e^{-\frac{i}{\hbar} \langle k | H' | k \rangle t} c_k(0) + e^{-\frac{i}{\hbar} \langle k | H' | k \rangle t} \times \\ \times \sum_{k'} c_k(t=0) \frac{e^{-it(E_k - E_{k'} - \langle k | H' | k \rangle)/\hbar} - 1}{E_k - E_{k'} - \langle k | H' | k \rangle} \langle k | H' | k' \rangle. \end{aligned}$$

We would now want to take the disorder average of $|c_k(t)|^2$. First we recall that $|k\rangle = \frac{1}{\sqrt{N}} \sum_n e^{-ikna} |n\rangle$, and therefore

$$\begin{aligned} \langle k'' | H' | k \rangle \langle k | H' | k' \rangle = \\ \frac{1}{N^2} \sum_{n, n'} w_n w_{n'} e^{i(k'' - k)n' a + i(k - k')na}. \end{aligned}$$

Using the fact that $\langle w_n w_{n'} \rangle = \frac{w^2}{3} \delta_{n, n'}$ (disorder average), we find

$$\langle \langle k'' | H' | k \rangle \langle k | H' | k' \rangle \rangle = \frac{w^2}{3} \frac{1}{N} \delta_{k'', k'}. \quad (\text{E6})$$

Using this, we obtain

$$\begin{aligned} \langle |c_k(t)|^2 \rangle - |c_k(0)|^2 = \\ \frac{w^2}{3} \frac{1}{N} \sum_{k' \neq k} |c_{k'}(t=0)|^2 \left| \frac{e^{-it(E_k - E_{k'})/\hbar} - 1}{E_k - E_{k'}} \right|^2, \quad (\text{E7}) \end{aligned}$$

where we note that the cross-terms vanished since $\langle \langle k'' | H | k \rangle \rangle = 0$. For small t we have

$$\langle |c_k(t)|^2 \rangle \approx |c_k(0)|^2 + \frac{t^2 w^2}{\hbar^2} \frac{1}{3} \frac{1}{N}. \quad (\text{E8})$$

Since the spectrum contains an imaginary term, for large t we will see an exponential growth. However, between the polynomial behavior observed above for small times and the exponential growth regime, there may be an intermediate time regime where $\langle |c_k(t)|^2 \rangle$ stabilize at a certain value. We can estimate the

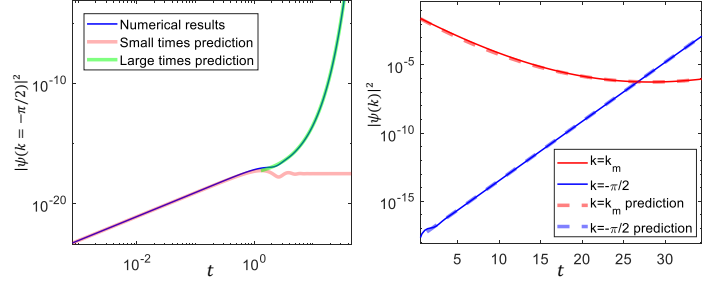


FIG. 12. Left panel: The numerical results versus the approximations for small and large times. Right panel: The numerical results of the maximum of the wave-packet (in red), and the numerical results for $k = -\pi/2$, versus their approximations (in dotted lines). The setup is the same as in Fig. 6.

saturation value by neglecting $\text{Im}[E_k - E_{k'}]$, so that Eq. (E7) becomes

$$\begin{aligned} \langle |c_k(t)|^2 \rangle - |c_k(0)|^2 \approx \\ \frac{w^2}{3} \frac{1}{N} \sum_{k'} |c_{k'}(t=0)|^2 \left[\frac{\sin(\frac{t}{2\hbar} \text{Re}(E_k - E_{k'}))}{\text{Re}(E_k - E_{k'})} \right]^2, \quad (\text{E9}) \end{aligned}$$

where we note that the approximation is true up to intermediate values of t . The saturation will occur when the sine function becomes of order unity, so we get that the saturation value is

$$\langle |c_k(t=t_s)|^2 \rangle \approx |c_k(0)|^2 + 4 \frac{w^2}{3} \frac{1}{N} \frac{1}{\text{Re}(E_k - E_{k_0})^2}, \quad (\text{E10})$$

and the saturation time is

$$t_s \approx \frac{\pi}{\text{Re}(E_k - E_{k_0})}, \quad (\text{E11})$$

where we also assumed that $c_k(t=0) \propto e^{-\sigma^2(k - k_0)^2}$, so that only $k' \approx k_0$ will contribute to the sum. Plugging in $k_0 = \frac{\pi}{4}$ and $k = -\pi/2$, we get that

$$\langle |c_{k=-\pi/2}(t=t_s)|^2 \rangle \approx \frac{8}{3} \frac{w^2}{N} \frac{1}{(t_r + t_l)^2}, \quad t_s \approx \frac{\pi\sqrt{2}}{(t_r + t_l)^2}. \quad (\text{E12})$$

Now, to get an estimation for large times, we can finally use the expression

$$\langle |c_{k=-\pi/2}(t)|^2 \rangle \approx \frac{8}{3} \frac{w^2}{N} \frac{1}{(t_r + t_l)^2} e^{2(t_l - t_r)(t - t_s)}. \quad (\text{E13})$$

In the left panel of Fig. 12 we compare Eq. (E9), (E13) with the numerical results, and see that they provide a very good approximation to the behavior of $\langle |c_{k=-\pi/2}(t)|^2 \rangle$ for small and large times, respectively.

We can now find the transition time between the Gaussian wave-packet to the wave-packet corresponding

to the maximum growth ($k = -\pi/2$). In order to do so, we need to find the time where the maximum magnitude of the Gaussian wave-packet becomes equal to the $k = -\pi/2$ packet. For $k = -\pi/2$, we will use our approximation from Eq. (E13). As for the maximum of the Gaussian wave-packet, in order to simplify the equations we will use the continuum limit given by Eq. (C9), which, as we have seen, is a good approximation up to moderate times. The spectrum is therefore

$$E = \frac{k^2}{2m} + ikb, \quad (\text{E14})$$

where in our case (since $a = 1$), b, m are given by

$$m = \frac{1}{2\sqrt{t_l t_r}}, \quad b = \ln\left(\frac{t_r}{t_l}\right) \sqrt{t_l t_r}. \quad (\text{E15})$$

Thus, we have

$$\psi(k, t) = \left(\frac{8\pi\sigma^2}{N^2}\right)^{1/4} e^{-\sigma^2(k-k_0)^2} e^{-i\left(\frac{k^2}{2m} + ikb\right)t}. \quad (\text{E16})$$

By completing the square, we get that

$$|\psi(k, t)|^2 = \left(\frac{8\pi\sigma^2}{N^2}\right)^{1/2} e^{2k_0 bt + \frac{b^2}{2\sigma^2} t^2} e^{-2\sigma^2[k - (k_0 + \frac{1}{2} \frac{b}{\sigma^2} t)]^2}, \quad (\text{E17})$$

so that the maximum amplitude is given by

$$|\psi(k_m, t)|^2 = \left(\frac{8\pi\sigma^2}{N^2}\right)^{1/2} e^{2k_0 bt + \frac{b^2}{2\sigma^2} t^2}. \quad (\text{E18})$$

That is, to determine the transition time due to disorder, we need to find when Eq. (E13) equals Eq. (E18). This yields a simple quadratic equation, and its solution gives the transition time. In the right panel of Fig. (12) we present the numerical results for the amplitude of $k = k_m$ and $k = -\pi/2$, and show that they are in a good agreement with the approximations in Eq. (E13), (E18).

a. The critical width $\sigma_{c,\text{dis}}$

As discussed in the main text, the transition can only be observed within a specific range of values for σ, w . Specifically, we show in Fig. 13 (14) that for a fixed w (σ), there is a critical value for σ (w).

Appendix F: Additional results in the non-Hermitian SSH model

In this section, we briefly discuss the dynamics of the non-Hermitian SSH model (Eq. (31)) using an initial Gaussian wave-packet. Fig. 15 illustrates the wave-packet dynamics in the non-Hermitian SSH model, both with and without the transformation given in Eq. (32). In the Hermitian case, the wave-packet splits into two

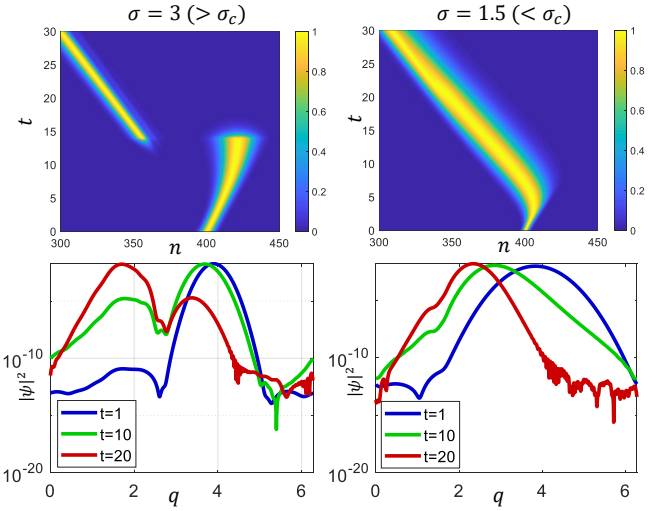


FIG. 13. Top panels: The transition for $w = 10^{-4}$ and two different values of σ (below and above the critical value). Bottom panels: The wave-packet in q -space for at three different times, $t = 1, 10, 20$. Except for σ, w , the setup is the same as in Fig. 6.

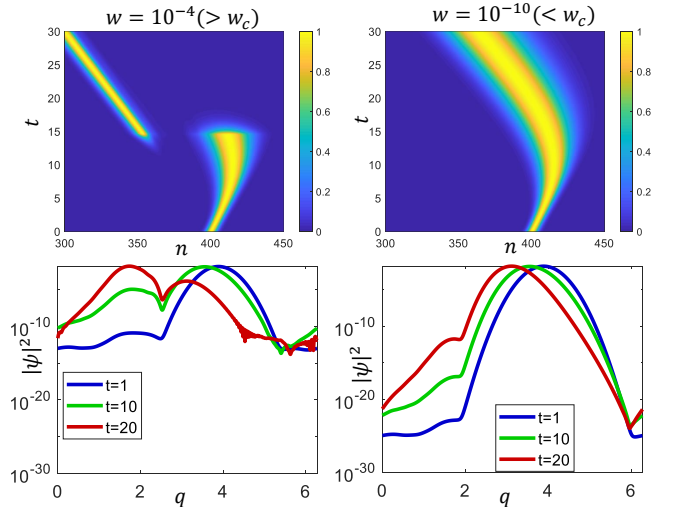


FIG. 14. Top panels: The transition for $\sigma = 2.5$ and two different values of w (below and above the critical value). Bottom panels: The wave-packet in q -space for at three different times, $t = 1, 10, 20$. Except for σ, w , the setup is the same as in Fig. 6.

Gaussians moving in opposite directions. In the non-Hermitian model, we also observe two Gaussian wave-packets, where each of them could be investigated by similar tools that were used in Sec. III. That is, each one of them will accelerate to the left before saturating at a finite velocity. However, due to the non-Hermiticity of the model, the leftward-moving packet is amplified, making the rightward-moving packet challenging to observe (at least for $n < n_0$), as shown in the figure.

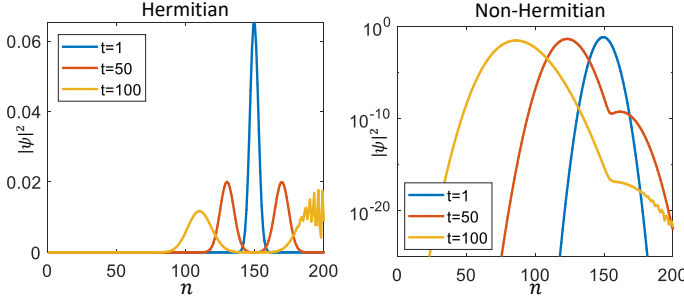


FIG. 15. The dynamics of the Hermitian (left panel) and non-Hermitian (right panel) wave-packets (with and without the transformation in Eq. (32)), in the non-Hermitian SSH model. The initial conditions are $\psi(n, A, t = 0) = \frac{1}{\sqrt{4\pi\sigma^2}} e^{-\frac{a^2(n-n_0)^2}{4\sigma^2} + ik_0 an}$ and $\psi(n, B, t = 0) = 0$, and the results are presented at 3 different times ($t = 1, 50, 100$). The parameters are $N = 200$, $a = 1$, $t_1 = 0.4$, $t_2 = 1$, $\gamma = 0.5$, $n_0 = 150$, $\sigma = 3$, and $k_0 = \pi/4$.

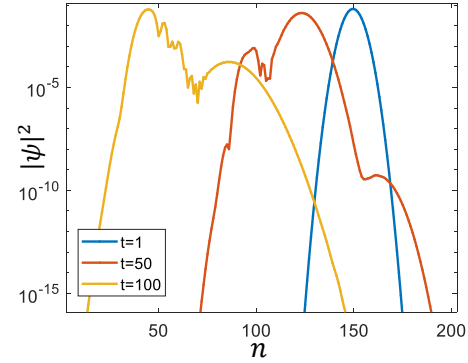


FIG. 16. The dynamics of the non-Hermitian SSH model with disorder. The setup is identical to that of Fig. 15, but with additional onsite disorder term with $w = 0.001$.

Specifically, the transition discussed in Sec. III B 2 (resulting from the reflection of the Hermitian wave) can also occur, but will be hard to observe. In contrast, disorder-induced transitions (like those investigated in Sec. III C) can easily be seen, as is shown in Fig. 16.

[1] C. M. Bender and S. Boettcher, Real spectra in non-hermitian hamiltonians having pt symmetry, *Physical Review Letters* **80** (1998).

[2] C. M. Bender, Making sense of non-hermitian hamiltonians, *Reports on Progress in Physics* **70**, 947 (2007).

[3] I. Rotter, A non-hermitian hamilton operator and the physics of open quantum systems, *Journal of Physics A: Mathematical and Theoretical* **42**, 153001 (2009).

[4] R. El-Ganainy, K. G. Makris, M. Khajavikhan, Z. H. Musslimani, S. Rotter, and D. N. Christodoulides, Non-hermitian physics and pt symmetry, *Nature Physics* **14**, 11 (2018).

[5] Y. Ashida, Z. Gong, and M. Ueda, Non-hermitian physics, *Advances in Physics* **69**, 249 (2020).

[6] M. Brandenbourger, X. Locsin, E. Lerner, and C. Coulais, Non-reciprocal robotic metamaterials, *Nature Communications* **10** (2019).

[7] A. Ghatak, M. Brandenbourger, J. van Wezel, and C. Coulais, Observation of non-hermitian topology and its bulk-edge correspondence in an active mechanical metamaterial, *Proceedings of the National Academy of Sciences* **117** (2020).

[8] A. Wang, Z. Meng, and C. Q. Chen, Non-hermitian topology in static mechanical metamaterials, *Science Advances* **9** (2023).

[9] R. Fleury, D. Sounas, and A. Alu, An invisible acoustic sensor based on parity-time symmetry, *Nature Communications* **6** (2015).

[10] K. Ding, G. Ma, M. Xiao, Z. Q. Zhang, and C. T. Chan, Emergence, coalescence, and topological properties of multiple exceptional points and their experimental realization, *Physical Review X* **6**, 021007 (2016).

[11] W. Zhu, X. Fang, D. Li, Y. Sun, Y. Li, Y. Jing, and H. Chen, Simultaneous observation of a topological edge state and exceptional point in an open and non-hermitian acoustic system, *Physical Review Letters* **121**, 124501 (2018).

[12] M. Wang, L. Ye, J. Christensen, and Z. Liu, Valley physics in non-hermitian artificial acoustic boron nitride, *Physical Review Letters* **120**, 246601 (2018).

[13] L. Zhang, Y. Yang, Y. Ge, Y.-J. Guan, Q. Chen, Q. Yan, F. Chen, R. Xi, Y. Li, D. Jia, S.-Q. Yuan, H.-X. Sun, H. Chen, and B. Zhang, Acoustic non-hermitian skin effect from twisted winding topology, *Nature Communications* **12** (2021).

[14] Z. Gu, H. Gao, P.-C. Cao, T. Liu, X.-F. Zhu, and J. Zhu, Controlling sound in non-hermitian acoustic systems, *Physical Review Applied* **16**, 057001 (2021).

[15] H. Gao, H. Xue, Z. Gu, T. Liu, J. Zhu, and B. Zhang, Non-hermitian route to higher-order topology in an acoustic crystal, *Nature Communications* **12** (2021).

[16] Q. Zhang, Y. Li, H. Sun, X. Liu, L. Zhao, X. Feng, X. Fan, and C. Qiu, Observation of acoustic non-hermitian bloch braids and associated topological phase transitions, *Physical Review Letters* **130**, 017201 (2023).

[17] K. Ding, Z. Q. Zhang, and C. T. Chan, Coalescence of exceptional points and phase diagrams for one-dimensional pt-symmetric photonic crystals, *Physical Review B* **92**, 235310 (2015).

[18] S. Longhi, D. Gatti, and G. D. Valle, Robust light transport in non-hermitian photonic lattices, *Scientific Reports* **5** (2015).

[19] B. Zhen, C. W. Hsu, Y. Igarashi, L. Lu, I. Kaminer, A. Pick, S.-L. Chua, J. D. Joannopoulos, and M. Soljacic, Spawning rings of exceptional points out of dirac cones,

Nature **525**, 354 (2015).

[20] L. Feng, R. El-Ganainy, and L. Ge, Non-hermitian photonics based on parity-time symmetry, Nature Photonics **11**, 752 (2017).

[21] M. Pan, H. Zhao, P. Miao, S. Longhi, and L. Feng, Photonic zero mode in a non-hermitian photonic lattice, Nature Communications **9** (2018).

[22] S. K. Ozdemir, S. Rotter, F. Nori, and L. Yang, Parity-time symmetry and exceptional points in photonics, Nature Materials **18**, 783 (2019).

[23] P. Peng, W. Cao, C. Shen, W. Qu, J. Wen, L. Jiang, and Y. Xiao, Anti-parity-time symmetry with flying atoms, Nature Physics **12**, 1139 (2016).

[24] J. Li, A. K. Harter, J. Liu, L. de Melo, Y. N. Joglekar, and L. Luo, Observation of parity-time symmetry breaking transitions in a dissipative floquet system of ultracold atoms, Nature Communications **10** (2019).

[25] Y. Takasu, T. Yagami, Y. Ashida, R. Hamazaki, Y. Kuno, and Y. Takahashi, Pt-symmetric non-hermitian quantum many-body system using ultracold atoms in an optical lattice with controlled dissipation, Progress of Theoretical and Experimental Physics **2020** (2020).

[26] Q. Liang, D. Xie, Z. Dong, H. Li, H. Li, B. Gadway, W. Yi, and B. Yan, Dynamic signatures of non-hermitian skin effect and topology in ultracold atoms, Physical Review Letters **129**, 070401 (2022).

[27] J. Schindler, A. Li, M. C. Zheng, F. M. Ellis, and T. Kottos, Experimental study of active lrc circuits with pt symmetries, Physical Review A **84**, 040101 (2011).

[28] M. De Carlo, F. De Leonidas, R. A. Soref, L. Colatorti, and V. M. N. Passaro, Non-hermitian sensing in photonics and electronics: A review, Sensors **22**, 3977 (2022).

[29] H. Yuan, Y. Cao, A. Kamra, R. A. Duine, and P. Yan, Quantum magnonics: When magnon spintronics meets quantum information science, Physics Reports **965**, 1 (2022).

[30] H. Shen and L. Fu, Quantum oscillation from in-gap states and a non-hermitian landau level problem, Physical Review Letters **121**, 026403 (2018).

[31] V. M. Martinez Alvarez, J. E. Barrios Vargas, and L. E. F. Foa Torres, Non-hermitian robust edge states in one dimension: Anomalous localization and eigenspace condensation at exceptional points, Physical Review B **97**, 121401 (2018).

[32] C. H. Lee and R. Thomale, Anatomy of skin modes and topology in non-hermitian systems, Physical Review B **99**, 201103 (2019).

[33] L. Li, C. H. Lee, S. Mu, and J. Gong, Critical non-hermitian skin effect, Nature Communications **11** (2020).

[34] N. Okuma, K. Kawabata, K. Shiozaki, and M. Sato, Topological origin of non-hermitian skin effects, Physical Review Letters **124**, 086801 (2020).

[35] D. S. Borgnia, A. J. Kruchkov, and R.-J. Slager, Non-hermitian boundary modes and topology, Physical Review Letters **124**, 056802 (2020).

[36] K. Zhang, Z. Yang, and C. Fang, Correspondence between winding numbers and skin modes in non-hermitian systems, Physical Review Letters **125**, 126402 (2020).

[37] X. Zhang, Y. Tian, J.-H. Jiang, M.-H. Lu, and Y.-F. Chen, Observation of higher-order non-hermitian skin effect, Nature Communications **12** (2021).

[38] D. Zou, T. Chen, W. He, J. Bao, C. H. Lee, H. Sun, and X. Zhang, Observation of hybrid higher-order skin-topological effect in non-hermitian topoelectrical circuits, Nature Communications **12** (2021).

[39] K. Zhang, Z. Yang, and C. Fang, Universal non-hermitian skin effect in two and higher dimensions, Nature Communications **13** (2022).

[40] R. Lin, T. Tai, L. Li, and C. H. Lee, Topological non-hermitian skin effect, Frontiers of Physics **18** (2023).

[41] F. K. Kunst, E. Edvardsson, J. C. Budich, and E. J. Bergholtz, Biorthogonal bulk-boundary correspondence in non-hermitian systems, Physical Review Letters **121**, 026808 (2018).

[42] H. Shen, B. Zhen, and L. Fu, Topological band theory for non-hermitian hamiltonians, Physical Review Letters **120**, 146402 (2018).

[43] L. Xiao, T. Deng, K. Wang, G. Zhu, Z. Wang, W. Yi, and P. Xue, Non-hermitian bulk-boundary correspondence in quantum dynamics, Nature Physics **16**, 761 (2020).

[44] O. Rapoport and M. Goldstein, Generalized topological bulk-edge correspondence in bulk-hermitian continuous systems with non-hermitian boundary conditions, Physical Review B **107**, 085117 (2023).

[45] S. Yao and Z. Wang, Edge states and topological invariants of non-hermitian systems, Physical Review Letters **121**, 086803 (2018).

[46] K. Yokomizo and S. Murakami, Non-bloch band theory of non-hermitian systems, Physical Review Letters **123**, 066404 (2019).

[47] E. J. Bergholtz, J. C. Budich, and F. K. Kunst, Exceptional topology of non-hermitian systems, Reviews of Modern Physics **93**, 015005 (2021).

[48] H. Li and S. Wan, Dynamic skin effects in non-hermitian systems, Physical Review B **106**, l241112 (2022).

[49] S. Longhi, Non-hermitian skin effect and self-acceleration, Physical Review B **105**, 245143 (2022).

[50] Z. Li, L.-W. Wang, X. Wang, Z.-K. Lin, G. Ma, and J.-H. Jiang, Observation of dynamic non-hermitian skin effects, Nature Communications **15** (2024).

[51] L. Li, W. X. Teo, S. Mu, and J. Gong, Direction reversal of non-hermitian skin effect via coherent coupling, Physical Review B **106**, 085427 (2022).

[52] N. Silberstein, J. Behrends, M. Goldstein, and R. Ilan, Berry connection induced anomalous wavepacket dynamics in non-hermitian systems, Phys. Rev. B **102**, 245147 (2020).

[53] B. Alon, R. Ilan, and M. Goldstein, Quantum metric dependent anomalous velocity in systems subject to complex electric fields, Phys. Rev. B **110**, 245103 (2024).

[54] B. Alon, M. Goldstein, and R. Ilan, The non-hermitian magnetic moment (2025), arXiv:2506.05206 [cond-mat.mes-hall].

[55] J. Behrends, R. Ilan, and M. Goldstein, Quantum geometry of non-hermitian systems (2025), arXiv:2503.13604 [quant-ph].

[56] S. Longhi, Probing non-hermitian skin effect and non-bloch phase transitions, Physical Review Research **1**, 023013 (2019).

[57] T. Lee and G. Wick, Negative metric and the unitarity of the s-matrix, Nuclear Physics B **9**, 209 (1969).

[58] A. MOSTAFAZADEH, Pseudo-hermitian representation of quantum mechanics, International Journal of Geometric Methods in Modern Physics **07**, 1191 (2010).

[59] A. Mostafazadeh, Pseudo-hermiticity versus pt-symmetry: The necessary condition for the reality of the spectrum of a non-hermitian hamiltonian, *Journal of Mathematical Physics* **43**, 205 (2002).

[60] A. Mostafazadeh, Pseudo-hermiticity versus pt-symmetry. ii. a complete characterization of non-hermitian hamiltonians with a real spectrum, *Journal of Mathematical Physics* **43**, 2814 (2002).

[61] A. Mostafazadeh, Pseudo-hermiticity versus pt-symmetry iii: Equivalence of pseudo-hermiticity and the presence of antilinear symmetries, *Journal of Mathematical Physics* **43**, 3944 (2002).

[62] R. Zhang, H. Qin, and J. Xiao, Pt-symmetry entails pseudo-hermiticity regardless of diagonalizability, *Journal of Mathematical Physics* **61** (2020).

[63] H. F. Jones, On pseudo-hermitian hamiltonians and their hermitian counterparts, *Journal of Physics A: Mathematical and General* **38**, 1741 (2005).

[64] W. P. Su, J. R. Schrieffer, and A. J. Heeger, Solitons in polyacetylene, *Physical Review Letters* **42**, 1698 (1979).

[65] S. Lieu, Topological phases in the non-hermitian schrieffer-heeger model, *Physical Review B* **97**, 045106 (2018).

[66] N. Hatano and D. R. Nelson, Localization transitions in non-hermitian quantum mechanics, *Physical Review Letters* **77**, 570 (1996).

[67] Adding phases of $e^{i\varphi}$ and $e^{-i\varphi}$ to t_r and t_l , respectively, preserves pseudo-Hermiticity, while any global phase does not.

[68] Advanpix LLC., *Multiprecision Computing Toolbox for MATLAB*, Yokohama, Japan.

[69] K. Schonhammer, Unusual broadening of wave packets on lattices, *American Journal of Physics* **87**, 186 (2019).

[70] We thus do not follow the terminology “inelastic scattering” introduced by Li and Wan (Ref. [48]).

[71] S. Weidemann, M. Kremer, S. Longhi, and A. Szameit, Coexistence of dynamical delocalization and spectral localization through stochastic dissipation, *Nature Photonics* **15**, 576-581 (2021).

[72] A. F. Tzortzakakis, K. G. Makris, A. Szameit, and E. N. Economou, Transport and spectral features in non-hermitian open systems, *Phys. Rev. Res.* **3**, 013208 (2021).

[73] A. Leventis, K. G. Makris, and E. N. Economou, Non-hermitian jumps in disordered lattices, *Phys. Rev. B* **106**, 064205 (2022).

[74] H. Sahoo, R. Vijay, and S. Majumdar, Anomalous transport regime in a non-hermitian anderson-localized hybrid system, *Phys. Rev. Res.* **4**, 043081 (2022).

[75] S. Longhi, Anderson localization in dissipative lattices, *Annalen der Physik* **535**, 10.1002/andp.202200658 (2023).

[76] E. T. Kokkinakis, K. G. Makris, and E. N. Economou, Anderson localization versus hopping asymmetry in a disordered lattice, *Phys. Rev. A* **110**, 053517 (2024).

[77] E. T. Kokkinakis, K. G. Makris, and E. N. Economou, Dephasing-induced jumps in non-hermitian disordered lattices, *Phys. Rev. B* **111**, 214204 (2025).

[78] E. T. Kokkinakis, I. Komis, K. G. Makris, and E. N. Economou, Non-hermitian off-diagonal disordered optical lattices (2025), arXiv:2512.07435 [cond-mat.dis-nn].

[79] We note that the single-site initial condition (orange line) exhibit some change at some time $t_3 < t < t_4$. This time equals to $\frac{2N+x_0}{v_h}$, which is the time it takes for the left-moving part of the wave-packet to hit the left wall, then the right wall, and then the left wall again. This part is suppressed in the Gaussian dynamics, since the Hermitian Gaussian is only moving to one direction, in contrast with the single-site initial condition, which generates two symmetrical wave-packets moving to the opposite directions.

[80] Y. He and T. Ozawa, Anomalous wave-packet dynamics in one-dimensional non-hermitian lattices (2025), arXiv:2512.07484 [physics.optics].